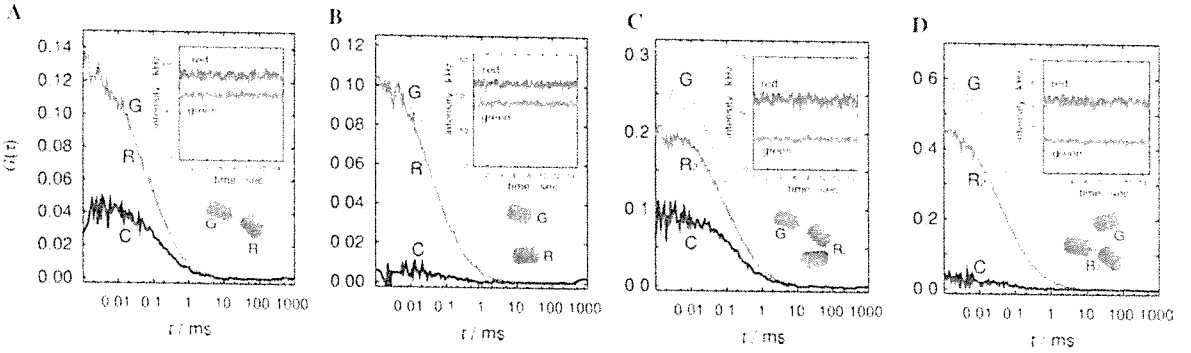

Fig. 1. In vitro cross-correlation analysis. Typical auto- and cross-correlation curves of (A) G-DEVD-R, (B) MixGR, (C) G-DEVD-R_2, and (D) MixGR$_2$ in PBS. (Insets) The fluorescence intensities in red and green channels during FCCS measurement. R, G, and C represent $G_r(\tau)$, $G_g(\tau)$, and $G_c(\tau)$, respectively. (For interpretation of the references to colours in this figure legend, the reader is referred to the web version of this paper.)

Table 1
Relative cross-correlation amplitude $G_c(0)/G_g(0)$

EGFP-mRFP chimera		Mixture of EGFP and mRFP	
Sample	$G_c(0)/G_g(0)$	Sample	$G_c(0)/G_g(0)$
In PBS			
G-DEVD-R	0.369 ± 0.006	MixGR	0.088 ± 0.002
G-DEVD-R_2	0.373 ± 0.007	MixGR$_2$	0.035 ± 0.006
In HeLa cells			
G-DEVD-R	0.467 ± 0.028	MixGR	0.233 ± 0.020
G-DEVD-R_2	0.391 ± 0.037	MixGR$_2$	0.102 ± 0.008
G-D_4K-R_2	0.394 ± 0.032	—	—
In apoptotic HeLa cells			
G-DEVD-R_2	0.047 ± 0.005	—	—
G-D_4K-R_2	0.237 ± 0.031	—	—

Values are means ± SD for three in vitro measurements and for six in vivo measurements.

concentration and smaller at a higher mRFP concentration (data not shown). We found that G-DEVD-R_2 is a sensitive probe compared to G-DEVD-R because the ratio of relative amplitude between G-DEVD-R_2 and MixGR$_2$ was higher than that of G-DEVD-R and MixGR (Table 1). By using auto-correlation analysis, it is impossible to distinguish G-DEVD-R_2 from MixGR$_2$ since the diffusion time of G-DEVD-R2 was only two times larger than that of MixGR2 (data not shown). We thus concluded that cross-correlation could clearly discriminate the difference of coincidence of linked FPs and unlinked FPs.

Real-time monitoring of protease reaction in vitro

In the EGFP-mRFP chimera, addition of protease should reduce cross-correlation amplitude $G_c(0)$. The protease reaction results in release of EGFP and mRFPs that may cause reduction of cross-correlation amplitude $G_c(0)$. Because N_r and N_g are constant during the protease reaction, $G_c(0)$ is directly proportional to the number of linked proteins N_c. The decrease of the intact G-D_4K-R_2 concentration could be monitored as a reduction of $G_c(0)/G_g(0)$. We thus measured how cross-correlation amplitude of G-D_4K-R_2 was altered upon addition of enterokinase (Fig. 2A). $G_c(0)$ of G-D_4K-R_2 was gradually reduced after adding 0.016 U/μl enterokinase. Fluorescence intensities in red and green channels were constant during the protease reaction (Fig. 2A, inset) and auto-correlation amplitudes $G_r(0)$ and $G_g(0)$ were also largely unchanged (data not shown). This suggested that no FRET occurred between EGFP and mRFP in intact G-D_4K-R_2 and also that the protease cleaved only the specific recognition sequence. $G_c(0)/G_g(0)$ of G-D_4K-R_2 was reduced to 20% and reached a plateau at 400 s after 0.016 U/μl enterokinase addition. We found that the reaction rate was proportional to the amount of the enzyme used (Fig. 2B). In contrast, no change of $G_c(0)/G_g(0)$ without enterokinase was observed. Then, the same time course as for FCCS measurements was used for real time monitoring of the cleavage process of 30 nM G-DEVD-R_2 after caspase-3 addition. $G_c(0)$ of G-DEVD-R_2 was slowly reduced after adding 1.0 U/μl caspase-3 at 37 °C (Fig. 2C). $G_c(0)/G_g(0)$ of G-DEVD-R_2 was reduced after adding caspase-3 (Fig. 2D) though the decay of $G_c(0)/G_g(0)$ of G-D_4K-R_2 was slower than that of G-DEVD-R2 at the same caspase-3 concentration. This demonstrated that the protease cleavage process could be simply monitored in real time by cross-correlation analysis as an 80% decrease of $G_c(0)$ in the small substrate concentration at a variable enzyme concentration (Fig. 2A) with specific recognition sequence (Fig. 2C).

In vivo control experiments

Next, we applied this strategy to the EGFP-mRFP chimera expressed in HeLa cells. At the beginning of measurements, strong photobleaching of mRFP occurred even at the same excitation laser power as in vitro. Consequently, the fluorescent intensity of the red channel decreased to about 1/3 and $G_r(0)$ increased about 3-fold

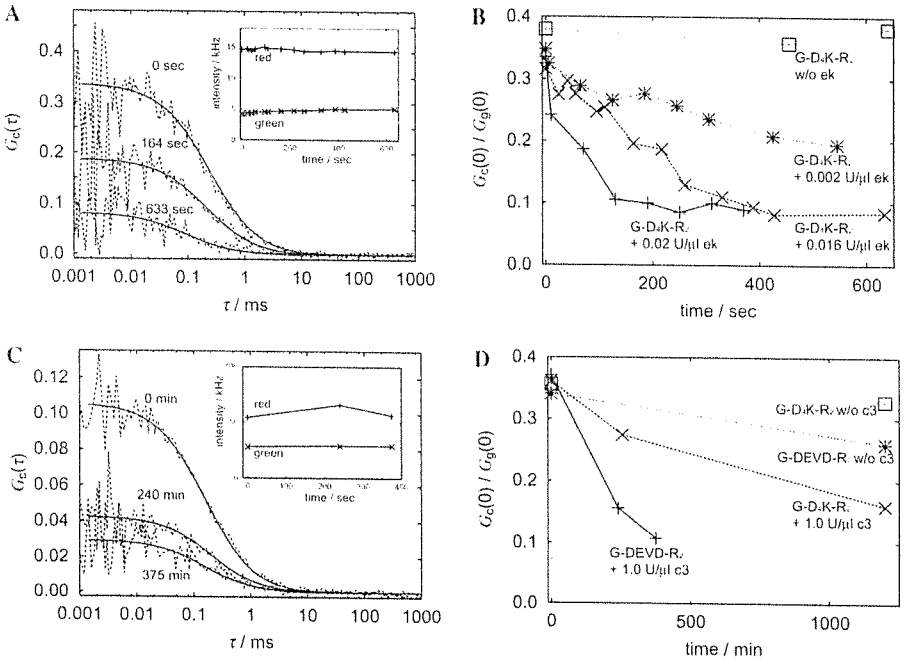

Fig. 2. Kinetics of protease reaction in vitro. (A) $G_c(\tau)$ of G-D_4K-R_2 in the time after 0.016 U/μl enterokinase addition. The dotted lines show measured curves and the solid lines show their fitted curves. (Inset) Time courses of the fluorescence intensities in red and green channels. (B) Relative cross-correlation amplitude, $G_c(0)/G_g(0)$ after the addition of various concentrations of enterokinase (ek). The concentration of G-D_4K-R_2 estimated from the amplitude of $G_g(\tau)$ was about 10 nM. (C) $G_c(\tau)$ of G-DEVD-R_2 in the time after 1.0 U/μl caspase-3 addition. The solid lines are measured curves and the dotted lines are their fitted curves. (Inset) Time courses of fluorescence intensities of red and green channels. (D) Relative cross-correlation amplitude, $G_c(0)/G_g(0)$ after the addition of caspase-3 (c3). Concentration of G-D_4K-R_2 estimated from the amplitude of $G_g(\tau)$ was about 30 nM. (For interpretation of the references to colours in this figure legend, the reader is referred to the web version of this paper.)

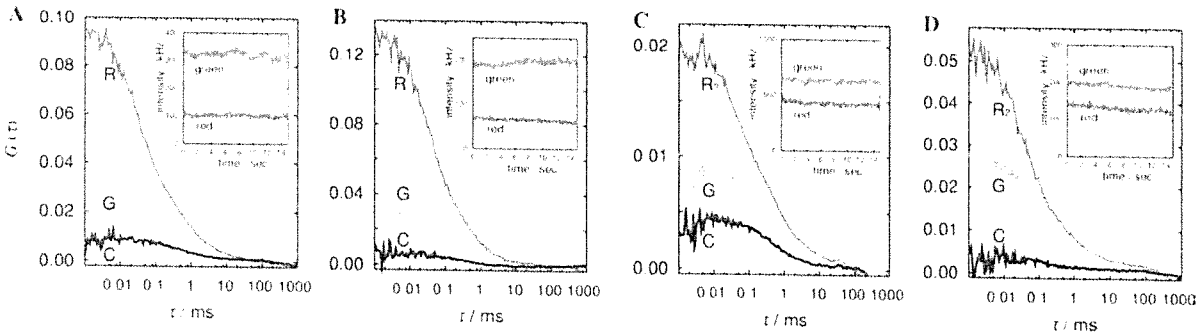

Fig. 3. Live cell cross-correlation analysis. Typical auto- and cross-correlation curves of (A) G-DEVD-R, (B) MixGR, (C) G-DEVD-R_2, and (D) MixGR_2 expressed in HeLa cells. (Insets) The fluorescence intensities in red and green channels during FCCS measurement. R, G, and C represent $G_r(\tau)$, $G_g(\tau)$, and $G_c(\tau)$, respectively.

(Fig. 3). In addition, $G_c(0)/G_g(0)$ of mixture of EGFP and mRFP, which indicates the background due to the red detector cross-talk, was larger than that of in vitro measurements (Table 1). These results were indicative of difficulties of in vivo measurements, however, we were able to obtain significant cross-correlation signal in a EGFP fused to a tandem mRFP dimer.

Detection of apoptosis-induced caspase-3 activation

To assess the potentials of this technique for biological application, we investigated FCCS-based detection of apoptosis-induced caspase-3 activation in vivo. For apoptosis induction, tumor necrosis factor-α (TNF-α), and cycloheximide (CHX) were loaded into HeLa cells. EGFP-mRFP chimera was distributed mostly in cytosol and also in the nucleus (Figs. 4A and C, insets). We selected cells which were weakly fluorescent to obtain sufficient amplitudes of auto-and cross-correlation. Cross-correlation signals of G-DEVD-R_2 and G-D_4K-R_2 in intact HeLa cells were same (Figs. 4A and C). Apoptotic morphological changes were observed at 3 h after TNF-α and CHX treatment (Figs. 4B and D, insets). In apoptotic HeLa cells, the cross-correlation

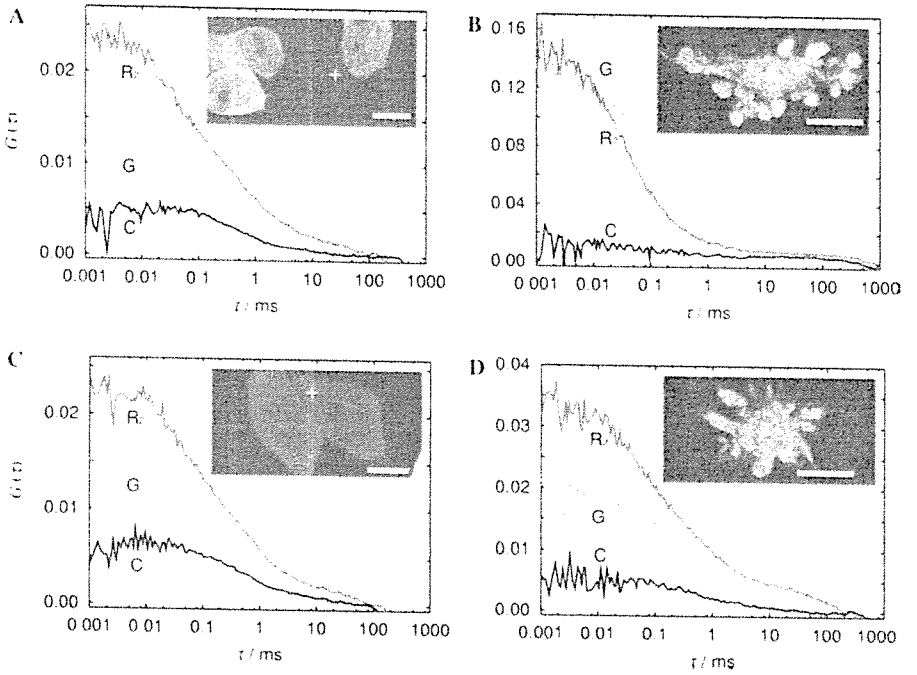

Fig. 4. Detection of caspase-3 activation in apoptotic HeLa cells. Typical auto- and cross-correlation spectroscopy of G-DEVD-R_2 (A) before and (B) after apoptosis induction and those of G-D_4K-R_2 (C) before and (D) after apoptosis induction in HeLa cells. (Insets) Measurement positions are indicated by the cross-hair (+) in the green channel laser scanning microscopy (LSM) images of G-DEVD-R_2 and G-D_4K-R_2 transiently expressed in HeLa cells. R, G, and C represent $G_r(\tau)$, $G_g(\tau)$, and $G_c(\tau)$, respectively. Scale bar represents 10 μm. (For interpretation of the references to colours in this figure legend, the reader is referred to the web version of this paper.)

amplitude of G-DEVD-R_2 was reduced (Fig. 4B). $G_c(0)/G_g(0)$ of G-DEVD-R_2 in apoptotic HeLa cells was as low as in the control, $G_c(0)/G_g(0)$ of MixGR_2 in intact HeLa cells (Table 1). On the other hand, even in apoptotic HeLa cells, the cross-correlation amplitude of G-D_4K-R_2 was maintained at a higher level because enterokinase was not distributed in the cell. While $G_c(0)/G_g(0)$ of G-D_4K-R_2 in apoptotic cells was slightly reduced, it was significantly higher than that of MixGR_2 in intact HeLa cells (Fig. 4D and Table 1). $G_c(0)/G_g(0)$ of G-D_4K-R_2 in apoptotic cells was somewhat reduced (Figs. 4C and D). It was also reduced by caspase-3 treatment in vitro (Fig. 2D). We thought the enterokinase site in the linker sequence (D_4K) is slightly susceptible to caspase-3. In apoptotic cells, there might be caspase-3, and also other protease activities induced by TNF-α. Finally, the DEVD sequence of G-DEVD-R_2 was selectively recognized by caspase-3 in live cells. These results indicate that cross-correlation analysis can detect the protease activation in vivo by the use of tandem mRFP dimer.

Discussion

By using the well-characterized proteolytic reaction of caspase-3, we have successfully showed that cross-correlation could clearly discriminate the difference of coincidence of linked FPs and unlinked FPs. We made the linker with the length in no FRET between EGFP and mRFP occurs because analysis of FCCS would be simplified. We did not try linker sequences with different lengths however we made enough length for the linker that did not inhibit the protease activity in this experiment. One of the advantages in the FCCS method is that FCCS is applicable to the sample with various (long or short) linker sequences. It was practically insensitive to detect the cleavage of FPs upon caspase-3 reaction by auto-correlation analysis. Assuming only one-direction cross-talk (green emission into red channel), in the case of EGFP-mRFP chimera, $G_c(0)$ is expected to be constant at single mRFP and double mRFPs from expanded equation of $G(0)$ [10]. On the other hand, in the case of mixture of EGFP and mRFP, $G_c(0)$ of double mRFPs is expected to be lower than single mRFP. Our results measured in PBS were consistent with these expectations (Table 1). The quantitative analysis as described here largely depends on the construction of stoichiometrically uniform probes in which different colored probe is fused to each other at a 1:1 ratio by conventional recombinant DNA technique [22]. Previously, it was reported that chemically synthesized probes, which were heterogeneously labeled, were not ideal for sensitivity of cross-correlation analysis [16]. However, since mRFP has relatively lower brightness and susceptibility to photobleaching [18], red-shifted improvement of this probe will be beneficial. When brighter, more red-shifted and photostable mRFP becomes available, FCCS will be one of the

most sensitive tools for in vivo biochemistry. Furthermore, FCCS can also be used to study the molecular interactions over long distances such as colocalization of cargoes in the same endocytic vesicles [16] and for the detection of a large DNA sample of 4 kbp 5′-Cy5 and 5′-rhodamine green-labeled PCR products [15]. FP-based FCCS may become the most versatile method for analysis of protein–protein interactions in live cells. We believe that this fluorescent protein-based FCCS will be a reliable fluorescence analysis for other intracellular protein dynamics and must become a powerful and convenient method for the analysis of protein–protein interactions in intact cells.

References

[1] A. Miyawaki, Visualization of the spatial and temporal dynamics of intracellular signaling, Dev. Cell 4 (2003) 295–305.

[2] R. Rigler, Ü. Mets, J. Widengren, P. Kask, Fluorescence correlation spectroscopy with high count rate and low background: analysis of translational diffusion, Eur. Biophys. J. 22 (1993) 169–175.

[3] Y. Takakuwa, C.-G. Pack, X.-L. An, S. Manno, E. Ito, M. Kinjo, Fluorescence correlation spectroscopy analysis of the hydrophobic interactions of protein 4.1 with phosphatidyl serine liposomes, Biophys. Chem. 82 (1999) 149–155.

[4] C.-G. Pack, K. Aoki, H. Taguchi, M. Yoshida, M. Kinjo, M. Tamura, Effect of electrostatic interactions on the binding of charged substrate to GroEL studied by highly sensitive fluorescence correlation spectroscopy, Biochem. Biophys. Res. Commun. 267 (2000) 300–304.

[5] P. Schwille, U. Haupts, S. Maiti, W.W. Webb, Molecular dynamics in living cells observed by fluorescence correlation spectroscopy with one- and two-photon excitation, Biophys. J. 77 (1999) 2251–2265.

[6] R.H. Köhler, P. Schwille, W.W. Webb, M.R. Hanson, Active protein transport through plastid tubules: velocity quantified by fluorescence correlation spectroscopy, J. Cell Sci. 113 (2000) 3921–3930.

[7] N. Yoshida, M. Kinjo, M. Tamura, Microenvironment of endosomal aqueous phase investigated by the mobility of microparticles using fluorescence correlation spectroscopy, Biochem. Biophys. Res. Commun. 280 (2001) 312–318.

[8] K. Saito, E. Ito, Y. Takakuwa, M. Tamura, M. Kinjo, In situ observation of mobility and anchoring of PKC/βI in plasma membrane, FEBS Lett. 541 (2003) 126–131.

[9] U. Kettling, A. Koltermann, P. Schwille, M. Eigen, Real-time enzyme kinetics monitored by dual-color fluorescence cross-correlation spectroscopy, Proc. Natl. Acad. Sci. USA 95 (1998) 1416–1420.

[10] R. Rigler, Z. Földes-Papp, F.-J. Meyer-Almes, C. Sammet, M. Völcker, A. Schnetz, Fluorescence cross-correlation: a new concept for polymerase chain reaction, J. Biotechnol. 63 (1998) 97–109.

[11] T. Winkler, U. Kettling, A. Koltermann, M. Eigen, Confocal fluorescence coincidence analysis: an approach to ultra high-throughput screening, Proc. Natl. Acad. Sci. USA 96 (1999) 1375–1378.

[12] T. Kohl, K.G. Heinze, R. Kuhlemann, A. Koltermann, P. Schwille, A protease assay for two-photon cross-correlation and FRET analysis based solely on fluorescent proteins, Proc. Natl. Acad. Sci. USA 99 (2002) 12161–12166.

[13] K. Korn, P. Gardellin, B. Liao, M. Amacker, Å. Bergström, H. Björkman, A. Camacho, S. Dörhöfer, K. Dörre, J. Enström, T. Ericson, T. Favez, M. Gösch, A. Honegger, S. Jaccoud, M. Lapczyna, E. Litborn, P. Thyberg, H. Winter, R. Rigler, Gene expression analysis using single molecule detection, Nucleic Acids Res. 31 (2003) 89.

[14] Z. Földes-Papp, M. Kinjo, K. Saito, H. Kii, T. Takagi, M. Tamura, J.M. Costa, E. Birch-Hirschfeld, U. Demel, P. Thyberg, G.P. Tilz, C677T single nucleotide polymorphisms of the human methylene tetrahydrofolate reductase and specific identification, Mol. Diagn. 7 (2003) 99–111.

[15] T. Takagi, H. Kii, M. Kinjo, DNA measurements by using fluorescence correlation spectroscopy and two-color fluorescence cross-correlation spectroscopy, Curr. Pharm. Biotech. 5 (2004) 199–204.

[16] K. Bacia, I.V. Majoul, P. Schwille, Probing the endocytic pathway in live cells using dual-color fluorescence cross-correlation analysis, Biophys. J. 83 (2002) 1184–1193.

[17] S.A. Kim, K.G. Heinze, M.N. Waxham, P. Schwille, Intracellular calmodulin availability accessed with two-photon cross-correlation, Proc. Natl. Acad. Sci. USA 101 (2004) 105–110.

[18] R.E. Campbell, O. Tour, A.E. Palmer, P.A. Steinbach, G.S. Baird, D.A. Zacharias, R.Y. Tsien, A monomeric red fluorescent protein, Proc. Natl. Acad. Sci. USA 99 (2002) 7877–7882.

[19] S.I. Choi, H.W. Song, J.W. Moon, B.L. Seong, Recombinant enterokinase light chain with affinity tag: expression from *Saccharomyces cerevisiae* and its utilities in fusion protein technology, Biotechnol. Bioeng. 75 (2001) 718–724.

[20] Y. Shi, Mechanisms of caspase activation and inhibition during apoptosis, Mol. Cell 9 (2002) 459–470.

[21] K. Madin, T. Sawasaki, T. Ogasawara, Y. Endo, A highly efficient and robust cell-free protein synthesis system prepared from wheat embryos: plants apparently contain a suicide system directed at ribosomes, Proc. Natl. Acad. Sci. USA 97 (2000) 559–564.

[22] A. Miyawaki, A. Sawano, T. Kogure, Lighting up cells: labelling proteins with fluorophores, Nat. Cell Biol. 5 (2003) S1–S7.

Molecular basis of the high-affinity activation of type 1 ryanodine receptors by imperatoxin A

Chul Won LEE*, Eun Hui LEE*, Koh TAKEUCHI†, Hideo TAKAHASHI†, Ichio SHIMADA†, Kazuki SATO‡, Song Yub SHIN§, Do Han KIM* and Jae Il KIM*[1]

*Department of Life Science, Kwangju Institute of Science and Technology, Kwangju 500-712, South Korea, †Graduate School of Pharmaceutical Sciences, The University of Tokyo, Tokyo 113-0033, Japan, ‡Department of Environmental Science, Fukuoka Women's University, Fukuoka 813-8529, Japan, and §Research Center for Proteineous Materials, Chosun University, Kwangju 501-759, South Korea

Both imperatoxin A ($IpTx_a$), a 33-residue peptide toxin from scorpion venom, and peptide A, derived from the II–III loop of dihydropyridine receptor (DHPR), interact specifically with the skeletal ryanodine receptor (RyR1), which is a Ca^{2+}-release channel in the sarcoplasmic reticulum, but with considerably different affinities. $IpTx_a$ activates RyR1 with nanomolar affinity, whereas peptide A activates RyR1 at micromolar concentrations. To investigate the molecular basis for high-affinity activation of RyR1 by $IpTx_a$, we have determined the NMR solution structure of $IpTx_a$, and identified its functional surface by using alanine-scanning analogues. A detailed comparison of the functional surface profiles for two peptide activators revealed that $IpTx_a$ exhibits a large functional surface area (approx. 1900 Å^2, where 1 Å = 0.1 nm), based on a short double-stranded antiparallel β-sheet structure, while peptide A bears a much smaller functional surface area (approx. 800 Å^2), with the five consecutive basic residues (Arg^{681}, Lys^{682}, Arg^{683}, Arg^{684} and Lys^{685}) being clustered at the C-terminal end of the α-helix. The functional surface of $IpTx_a$ is composed of six essential residues (Leu^7, Lys^{22}, Arg^{23}, Arg^{24}, Arg^{31} and Arg^{33}) and several other important residues (His^6, Lys^8, Arg^9, Lys^{11}, Lys^{19}, Lys^{20}, Gly^{25}, Thr^{26}, Asn^{27} and Lys^{30}), indicating that amino acid residues involved in RyR1 activation make up over the half of the toxin molecule with the exception of cysteine residues. Taken together, these results suggest that the site where peptide A binds to RyR1 belongs to a subset of macrosites capable of being occupied by $IpTx_a$, resulting in differing the affinity and the mode of activation.

Key words: excitation–contraction coupling, imperatoxin A, NMR, peptide A, ryanodine receptor, solution structure.

INTRODUCTION

In cardiac and skeletal muscle, the ryanodine receptor (RyR) is a Ca^{2+}-release channel in the sarcoplasmic reticulum (SR) and the dihydropyridine receptor (DHPR) is a voltage-gated L-type Ca^{2+} channel. These two receptors play central roles in the sarcolemma excitation–contraction (E–C) coupling that links an electrical stimulus (depolarization) to release of Ca^{2+} from the SR [1]. Cardiac and skeletal muscles express different subtypes of DHPRs and RyRs, causing tissue-specific E–C coupling. In cardiac muscle, E–C coupling is induced by the entry of extracellular Ca^{2+} through DHPR, whereas skeletal type E–C coupling requires a direct physical coupling between DHPR and RyR [2,3]. Evidence supporting this physical coupling between skeletal DHPR and RyR1 (skeletal type RyR) includes successful co-immunoprecipitation [4] and identification of regions involved in the physical coupling between the two channels. Specifically, interactions have been observed between portions of the α_1 subunit of DHPR, including the II–III loop, the III–IV loop and the C-terminal segment, and the Arg^{1076}–Asp^{1112} region of RyR1 [5–12]. It has been proposed that these interactions cause orthograde signalling from DHPR to RyR1 for activation of RyR1, and retrograde signalling from RyR1 to DHPR for RyR1-mediated enhancement of Ca^{2+} current [11,13].

Imperatoxin A ($IpTx_a$), a 33-amino-acid peptide from the venom of the scorpion, *Pandinus imperator*, was the first peptide toxin found to activate RyR1 with high potency and affinity, and it has been used in several biochemical and biophysical studies related to the E–C coupling [14,15]. Interestingly, it has been suggested that $IpTx_a$ activates RyR1 by mimicking a domain of DHPR that is critical for triggering Ca^{2+} release. Using synthetic peptides corresponding to small segments of the II–III loop in skeletal DHPR, El-Hayek et al. [7] found that only the N-terminal portion (peptide A; Thr^{671}–Leu^{690}) was capable of activating RyR1, and subsequently identified a ten-residue active region (Arg^{681}–Leu^{690}) [16]. In addition, Gurrola et al. [17] reported that a peptide A-containing segment (Glu^{666}–Leu^{690}) might bind to the same RyR1 site as $IpTx_a$, as shown by the results of competitive binding of ^{125}I-labelled $IpTx_a$ to the SR. This was additionally supported by the report that both peptides produced almost identical changes, with non-additive effects, in RyR1 gating characteristics [18]. Although these observations strongly suggested that $IpTx_a$ and peptide A share a common binding site on RyR1, the two peptide activators show very low sequence identity (approx. 18%), very different molecular structures, and considerably different affinities in RyR1 activation. $IpTx_a$ activates RyR1 with nanomolar affinity, whereas peptide A activates RyR1 at micromolar concentrations [17].

In order to examine the molecular basis by which two peptide activators, $IpTx_a$ and peptide A, act at a common site on RyR1 with different affinities, the present study reports the solution structure of $IpTx_a$ as determined by NMR spectroscopy and

Abbreviations used: ω-CTX, ω-conotoxin; DHPR, dihydropyridine receptor; DQF-COSY, double-quantum-filtered COSY; E–C, excitation–contraction; Fmoc, 9-fluorenylmethoxycarbonyl; HOHAHA, homonuclear Hartmann–Hahn; $IpTx_a$, imperatoxin A; $w$$IpTx_a$, wild-type $IpTx_a$; NOE, nuclear Overhauser effect; PEG, poly(ethylene glycol); RyR, ryanodine receptor; RMSD, root mean square difference; RyR1, skeletal RyR; SR, sarcoplasmic reticulum.

[1] To whom correspondence should be addressed (e-mail jikim@kjist.ac.kr).

The co-ordinates of $IpTx_a$ have been deposited in the RCSB (Research Collaboratory for Structural Bioinformatics) Protein Data Bank under the accession code 1IE6.

dynamic simulated annealing calculations, and we have combined this structural information with the results of [^{3}H]ryanodine binding assays using alanine-scanning analogues. On the basis of the structure–activity relationships for IpTx$_a$, we propose that the peptide A-binding site on RyR1 belongs to a subset of macrosites capable of being occupied by IpTx$_a$, resulting in the observed differences in RyR1 affinity and activation. Furthermore, a comparative structural analysis with the cone-snail ω-conotoxin MVIIC (ω-CTX-MVIIC), a neuronal P/Q-type calcium-channel blocker, revealed that the characteristic shape of charged surface rather than globular shape is important to the interaction with RyR1, thus providing a structural insight for the specific interaction mode of RyR1-targeting peptide effectors.

MATERIALS AND METHODS

Materials

Fmoc (9-fluorenylmethoxycarbonyl) amino acids and other reagents used for peptide synthesis were obtained from Applied Biosystems. Fmoc-preloaded resin was obtained from Watanabe Chemical Industries (Hiroshima, Japan). [^{3}H]ryanodine was obtained from NEN Life Science Products (Torrance, CA, U.S.A.). All other regents were of high-purity reagent grade from Sigma Chemical Co.

Peptide synthesis of wild-type IpTx$_a$ (*w*IpTx$_a$) and analogues

Peptide synthesis was conducted on an Applied Biosystems model 433A peptide synthesizer. The linear precursors of *w*IpTx$_a$ and alanine-scanning analogues were synthesized by solid-phase Fmoc chemistry starting from Fmoc-Arg(2,2,5,7,8-pentamethylchroman-6-sulphonyl)-Alko or Fmoc-Ala-Alko resin and using a variety of blocking groups for amino acid protection. After cleavage by trifluoroacetic acid, crude linear peptides were extracted with 2 M ethanoic acid, diluted to final peptide concentrations of 25 μM in a solution of 1 M ammonium acetate and 2.5 mM reduced/0.25 mM oxidized glutathione adjusted to pH 7.8 with aqueous NH_4OH, and stirred slowly at 4 °C for 2–3 days. The folding reactions were monitored by HPLC. The crude oxidized products were purified by successive chromatography with CM-cellulose CM-52 and preparative HPLC with C_{18} silica columns. The purity of all analogues was confirmed by analytical HPLC and MALDI–TOF-MS (matrix-assisted laser-desorption ionization–time-of-flight MS) measurements.

CD measurements of *w*IpTx$_a$ and analogues

CD spectra were measured on a JASCO J-750 spectropolarimeter in solution (0.01 M sodium phosphate in water, pH 7.0) at 20 °C with a quartz cell of path length 1 mm. The spectra were expressed as molecular ellipticity [θ] in deg · cm^2 · dmol^{-1}.

NMR measurements of *w*IpTx$_a$

NMR spectra were recorded on a Bruker DRX 600 spectrometer. All two-dimensional NMR experiments {i.e. DQF-COSY (double-quantum-filtered COSY) [19], E-COSY (exclusive COSY) [20], HOHAHA (homonuclear Hartmann–Hahn) [21] and NOESY [22]} were performed with standard pulse sequences and phase cycling. HOHAHA spectra were recorded with mixing times of 60 and 80 ms. NOESY spectra were recorded with mixing times of 100, 200 and 300 ms. In all experiments, 512 increments of 2048 data points were recorded with 64–128 transients and were zero-filled once along the t_1 dimension. A complete set of the two-dimensional spectra was recorded at 27 °C (pH 3.4). Synthesized *w*IpTx$_a$ (a final concentration of 5 mM) was dissolved in 0.2 ml of water containing ^2H_2O at 10 % (v/v) or 99.9 % (v/v). Spectra were processed and analysed with Bruker XWIN-NMR software.

Structure calculations of *w*IpTx$_a$

Observed NOE (nuclear Overhauser effect) data were classified into four distance ranges, 1.8–2.7, 1.8–3.5, 1.8–5.0 and 1.8–6.0 Å (1 Å = 0.1 nm), corresponding to strong, medium, weak and very weak NOE values respectively. Pseudo-atoms were used for the methyl protons or the non-stereospecifically assigned methylene protons [23]. Correcting factors for the use of pseudo-atoms were added to the distance constraints. In addition, 0.5 Å was added to the distance constraints involving methyl protons [24]. For each disulphide bond, three distance constraints, S(i)-S(j), S(i)-C$^\beta$(j) and S(j)-C$^\beta$(i), were used with target values set to 2.02($\pm$0.02), 2.99($\pm$0.5) and 2.99($\pm$0.5) Å respectively [25].

All calculations were performed using the X-PLOR 3.1 program [26] running on a SGI O2 workstation. Three-dimensional structures were calculated on the basis of distance and torsion angle constraints experimentally derived with dynamic simulated annealing protocols. The 20 best structures were chosen for structural analysis, based on the X-PLOR energy and best fit. The structures were analysed with the PROCHECK-NMR [27] and PROMITIF [28] software packages. Structural figures were generated with the MOLMOL program [29] and the INSIGHT II 2000 program (Accelrys Inc.).

Isolation of SR vesicles

A heavy fraction of SR was prepared from rabbit back and leg fast twitch muscles with a modification of the previously described method [30]. Briefly, about 150 g of muscle was homogenized in a Waring blender with 4 vol. of 2.5 mM NaOH for six bursts of 20 s at intervals of 3 min. During the homogenization, the pH was adjusted to 6.8 with NaOH. The suspension was centrifuged at 10000 *g* for 3 min in a No. 9 rotor in a Hanil Supra22K centrifuge. The supernatant was filtered through eight layers of cheesecloth and then through Whatman filter paper (No. 4). After re-adjusting the pH to 6.8, if necessary, the filtrate was centrifuged again at 17000 *g* for 30 min in the above apparatus. The pellets were suspended in the final buffer consisting of 0.15 M KCl, 20 mM Mops (pH 6.8) and 0.3 M sucrose in the presence of the following protease inhibitors: pepstatin (1 μM), leupeptin (1 μM), PMSF (100 μM) and trypsin inhibitor (1 μM). The suspension was centrifuged again at 17000 *g* for 30 min in a No. 7 rotor in a Hanil Supra22K centrifuge. The pellets were resuspended in the same final buffer and the final protein concentration was determined by the Bradford method [30a] using BSA as the standard. The obtained SR was quickly frozen in liquid N_2 and then stored at −70 °C until use.

[^{3}H]Ryanodine binding assay with *w*IpTx$_a$ and analogues

[^{3}H]Ryanodine binding to rabbit skeletal SR vesicles was performed as previously described [31] with some modifications. Briefly, 0.04 mg of skeletal SR vesicles was incubated with various concentrations of *w*IpTx$_a$, or one of the analogues, for 2 h at 37 °C in a reaction mixture of 250 μl {0.2 M KCl, 20 mM Mops (pH 7.3), 5 nM [^{3}H]ryanodine and 10 μM free Ca^{2+}}. After incubation, 100 μl of poly(ethylene glycol) (PEG) solution (30 %

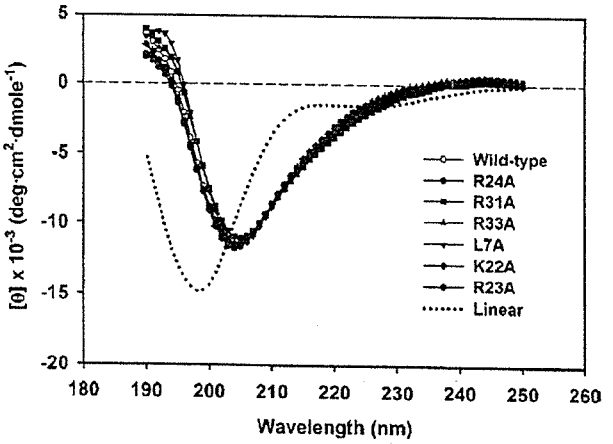

Figure 1 CD spectra of *w*IpTx$_a$ and its analogues

The measurement was carried out in the UV range of 250–190 nm on a JASCO J-750 spectropolarimeter in solution (0.01 M sodium phosphate, pH 7.0) at 20 °C.

PEG, 1 mM EDTA and 50 mM Tris, pH 7.3) was added to each vial and was incubated for 5 min at room temperature (25 °C). Precipitated protein was sedimented for 5 min at 12 000 *g* using an Eppendorf microcentrifuge, and the pellets were rinsed twice with 0.6 ml of the relevant ryanodine-binding buffer without radioactive ryanodine. The pellets were then solubilized in 100 μl of Soluene 350 (Packard) at 70 °C for 30 min, after which 4 ml of cocktail [Picofluor (Packard)] was added and the radioactivity was measured by liquid scintillation [32]. To minimize non-specific binding, 100-fold of non-radioactive ryanodine (Calbiochem) was included.

Statistical analysis

Results are given as means ± S.E.M. with the number of experiments. The S.E.M. is included within the Figure legends or indicated by error bars. Individual activation curves of RyR1 by *w*IpTx$_a$ and analogues were fitted with the Hill equation using the Origin 4.1 software package (RockWare, Golden, CO, U.S.A.).

RESULTS AND DISCUSSION

Synthesis of *w*IpTx$_a$ and analogues

Linear precursors of *w*IpTx$_a$ and its alanine-scanning analogues were assembled by solid-phase methodology. The crude linear precursors were air-oxidized, and the properly folded products were purified by ion-exchange chromatography and reverse-phase HPLC (1–4% yield from the starting resin). CD spectra showed that secondary structures of all analogues, including L7A (Leu^7 → Ala), K22A (Lys^{22} → Ala), R23A (Arg^{23} → Ala), R24A (Arg^{24} → Ala), R31A (Arg^{31} → Ala) and R33A (Arg^{33} → Ala), were similar to that of *w*IpTx$_a$ (Figure 1). Exceptionally, the linear analogue (Ala^{3,10,16,17,21,32})IpTx$_a$, which simultaneously replaced all six cysteine residues with alanine residues, showed a random conformation with a large negative Cotton effect (around 198 nm), indicating that the three intramolecular disulphide bonds in *w*IpTx$_a$ play an important role in maintaining its overall structure.

Structure calculations of *w*IpTx$_a$

Complete proton assignments of all 33 amino acids in synthetic *w*IpTx$_a$ were determined using traditional two-dimensional NMR sequential assignment techniques [33]. Identification of the amino acid spin system was based on scalar coupling patterns observed in DQF-COSY and HOHAHA experiments, complemented with the results of NOESY measurements. Figure 2 shows the NH-C$^\alpha$H

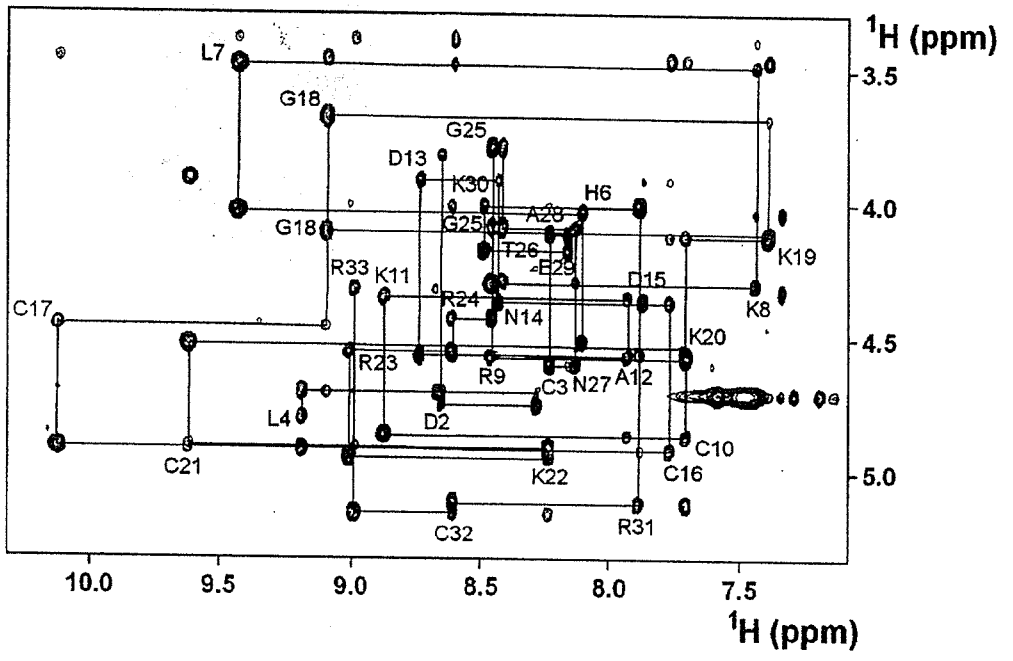

Figure 2 Sequential $d_{\alpha N}(i,i+1)$ NOE connectivity for residues 2–33 in the NOESY spectrum observed with a mixing time of 300 ms

Intra-residue NH-C$^\alpha$H cross-peaks are labelled with the residue numbers by standard single-letter amino acid abbreviations.

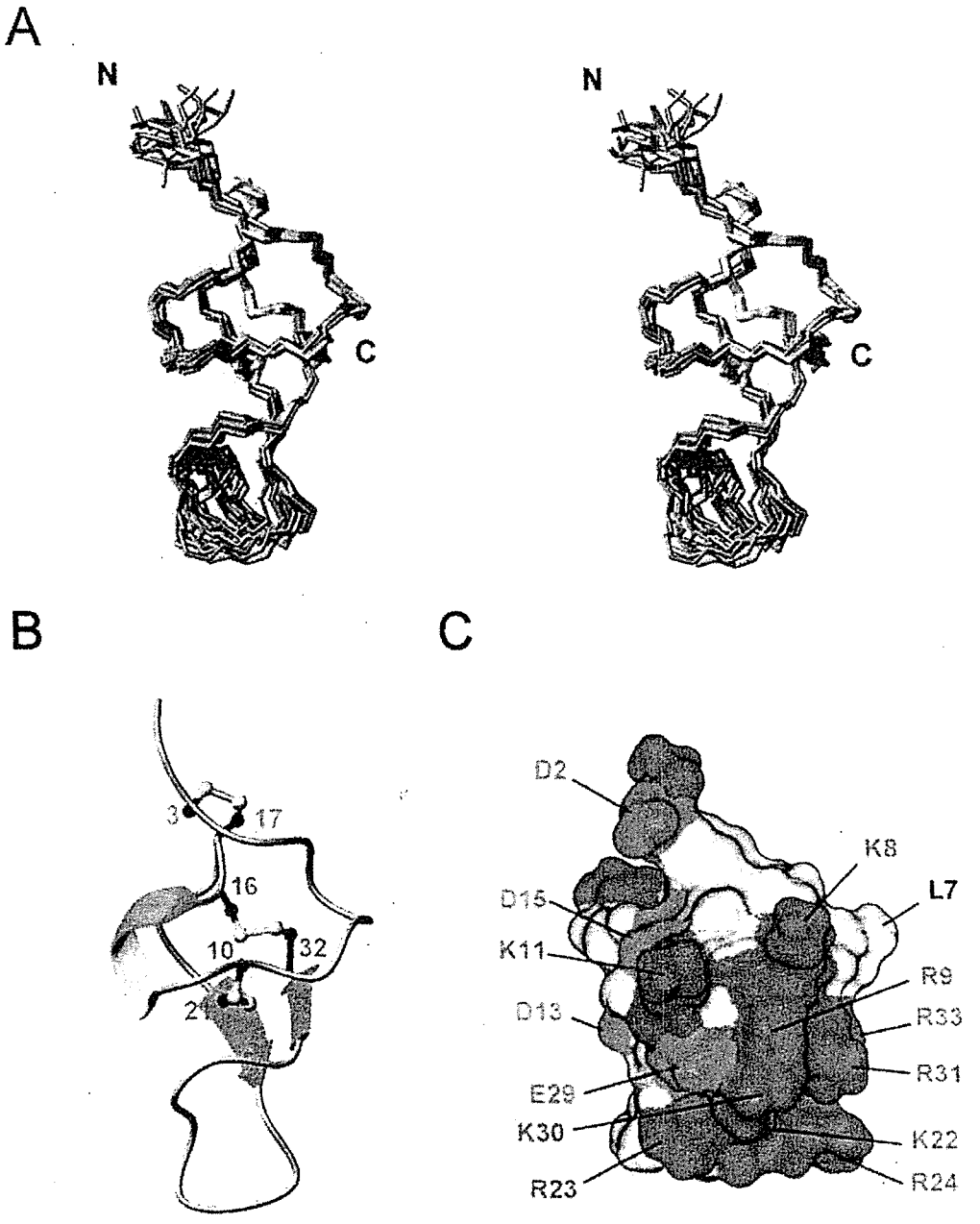

Figure 3 Solution structure of *w*IpTx$_a$

(**A**) Stereo view of the heavy atom backbone (N, C$^\alpha$, C) for the 20 converged structures of *w*IpTx$_a$, which are superimposed for the best fit over the heavy atom backbone (residues Cys^3–Arg^{23} and residues Lys^{30}–Cys^{32}). Disulphide bonds are shown in yellow. (**B**) Schematic diagram of *w*IpTx$_a$ illustrating the location of the β-strands (cyan), 3_{10}-helical turn (red and yellow) and disulphide bonds (numbered ball and stick in yellow). These Figures were generated using the MOLMOL program [29]. (**C**) Surface profile of *w*IpTx$_a$. The molecular surface of *w*IpTx$_a$ is shown in colour according to the electrostatic potential (negatively charged amino acids are in red, positively charged amino acids are in blue, and uncharged or hydrophobic amino acids are in white). Residues D2, L7, K8, R9, K11, D13, D15, K22, R23, R24, E29, K30, R31 and R33 (single-letter amino acid codes) are indicated.

fingerprint region of the NOESY spectrum, containing sequential $d_{\alpha N}(i,i+1)$ connectivity.

For the structure calculation of *w*IpTx$_a$, we used 473 distance constraints derived from the two-dimensional NOESY spectra, 25 dihedral angle constraints derived from the coupling constants and NOE measurements, 12 hydrogen-bond restraints derived from the hydrogen–deuterium exchange experiments [Cys^{10}(HN)–Lys^{30}(CO), Lys^{20}(HN)–Arg^{33}(CO), Lys^{22}(HN)–Arg^{31}(CO), Arg^{31}(HN)–Lys^{22}(CO), Cys^{32}(HN)–Lys^8(CO) and Arg^{33}(HN)–Lys^{20}(CO)] and nine additional disulphide-bond restraints for a total of 519 restraints, corresponding to an average of 15.7 constraints per residue. The disulphide-bond pattern of synthetic *w*IpTx$_a$ was determined to be Cys^3–Cys^{17}, Cys^{10}–Cys^{21} and Cys^{16}–Cys^{32} by combined approaches of enzyme

Table 1 Structural statistics for the 20 lowest-energy structures

None of these 20 structures exhibited distance violations > 0.5 Å or dihedral angle violations > 5°.

Property	Value
RMS deviations from experimental distance constraints (Å) (494)*	0.0395 ± 0.0017
RMS deviations from experimental dihedral constraints (°) (25)*	0.7879 ± 0.1200
Energetic statistics (kcal · mol^{-1})†	
F_{NOE}	38.4861 ± 3.2228
F_{tor}	0.9821 ± 0.3076
F_{repel}	12.9477 ± 2.7362
E_{L-J}	−61.8040 ± 9.3520
RMS deviations from idealized geometry	
Bonds (Å)	0.0036 ± 0.0002
Angles (°)	0.6279 ± 0.0198
Impropers (°)	0.4603 ± 0.0350
Ramachandran analysis (residues 3–23 and 30–32)‡	
Most favoured regions	67.5%
Additionally allowed regions	31.6%
Generously allowed regions	0.9%
Disallowed regions	0%
Average RMSD (Å)	
Backbone (N, C$^{\alpha}$, C) (residues 3–23 and 30–32)	0.38 ± 0.08
All heavy atoms (residues 3–23 and 30–32)	1.46 ± 0.26

* The number of each experimental constraint used in the calculations is given in parentheses.

† F_{NOE}, F_{tor} and F_{repel} are the energies related to the NOE violations, the torsion angle violations and the van der Waals repulsion term respectively. The values of the force constants used for these terms are the standard values as depicted in the X-PLOR 3.1 manual. E_{L-J} is the Lennard–Jones/van der Waals energy calculated with the CHARMm empirical energy function [56]. E_{L-J} was not used in the dynamic simulated annealing calculations.

‡ The program PROCHECK-NMR was used to assess the stereochemical quality of the structures.

fragmentation and chemical synthesis (C. W. Lee, E. H. Lee, T. Sasaki, K. Sato, K. Takeuchi, H. Takahashi, I. Shimada, D. H. Kim and J. I. Kim, unpublished work).

Structure description of *w*IpTx$_a$

Twenty structures with the lowest residual restraint violations were used to represent the three-dimensional structure of *w*IpTx$_a$ (Figure 3A). These structures have good non-bonded contacts as shown by low Lennard–Jones potential values, and a good covalent geometry, with only small deviations from the ideal bond lengths and bond angles (Table 1). There were no distance or dihedral angle restraint violations greater than 0.5 Å and 5° respectively. Excluding the final two residues of the N-terminus (Gly^1 and Asp^2) and the loop region from Arg^{24} to Glu^{29}, both of which were poorly defined by the NMR data, the average root mean square difference (RMSD) for the final 20 structures with respect to the mean co-ordinate positions was 0.38 ± 0.08 Å for the backbone atoms and 1.46 ± 0.26 Å for all heavy atoms. Structural statistics for the 20 converged structures of *w*IpTx$_a$ are summarized in Table 1.

The molecular structure of *w*IpTx$_a$ consists of two β-strands arranged in an antiparallel fashion, connected by four chain reversals (Figure 3B). The two β-strands are formed by residues Lys^{20}–Arg^{23} (β-strand I) and Lys^{30}–Arg^{33} (β-strand II). The first reversal occurs at residues Pro^5–Lys^8, which form a type IV β-turn (miscellaneous type). The second and third reversals occur at residues Asp^{13}–Asp^{15} and Cys^{16}–Lys^{19} and form a 3_{10} helical turn and a type I β-turn respectively. Both of these are contained within the external long loop between the first turn and β-strand I. The final reversal occurs between residues Arg^{24} and Glu^{29} and serves to reverse the backbone between β-strands I and II, without showing the characteristic distance pattern of a tight reverse turn. In terms of RMSD, this loop is poorly defined and presents the highest degree of structural disorder in the cysteine-rich region (Figure 3A).

The hydrophobic core of *w*IpTx$_a$ is entirely composed of the Cys^{10}, Cys^{16}, Cys^{21} and Cys^{32} side chains. The disulphide bond between Cys^{10} and Cys^{21} connects the second reversal to β-strand I, whereas the disulphide bonds between Cys^3 and Cys^{17} and between Cys^{16} and Cys^{32} connect the third reversal to the N-terminus and β-strand II respectively (Figure 3B). This pattern of disulphide connectivity is topologically classified as an 'inhibitor cystine knot' fold [34,35], in which the disulphide bond between Cys^{16} and Cys^{32} penetrates through a 13-residue ring formed by the peptide backbone and the other two disulphide bonds. Similar topology is frequently found in numerous toxic and inhibitory peptides, including the ω-conotoxins, ω-agatoxins and various protease inhibitors [36–42].

Structure–activity relationships of IpTx$_a$

The biological activities of synthetic *w*IpTx$_a$ and its 26 analogues were determined by examining their effects on RyR1 in SR vesicles from rabbit skeletal muscle, using a [^{3}H]ryanodine-binding assay. As shown in Figure 4, synthetic *w*IpTx$_a$ efficiently increased specific [^{3}H]ryanodine binding with EC_{50} = 28.40 ± 6.71 nM and B_{max} = 6.79 ± 0.30 pmol/mg of protein. The control binding of [^{3}H]ryanodine in the absence of *w*IpTx$_a$ was 0.57 ± 0.15 pmol/mg of protein. The specific [^{3}H]ryanodine binding in the presence of 30 nM of each analogue (corresponding to the apparent EC_{50} of *w*IpTx$_a$) is summarized in Figure 4(A). Interestingly, all analogues possessing alanine replacements for basic residues caused an apparent reduction of specific [^{3}H]ryanodine binding, whereas all analogues possessing alanine replacements for acidic residues showed slight increases of specific [^{3}H]ryanodine binding. In addition, the H6A (His^6 → Ala), L7A, G25A (Gly^{25} → Ala), T26A (Thr^{26} → Ala) and N27A (Asn^{27} → Ala) analogues also showed decreased [^{3}H]ryanodine binding. These results suggest that a large surface area on IpTx$_a$ contributes to activating RyR1, and that the integrity of electrostatic potential, together with other additional factors, affects RyR1 activation.

In order to evaluate the residues essential to RyR1 activation in detail, we examined the dose-dependent activation by all synthetic IpTx$_a$ analogues further. The EC_{50} values of all analogues are summarized in Table 2. Analysis of the dose effects showed that substituting residues at 16 positions, including positions 6, 7, 8, 9, 11, 19, 20, 22, 23, 24, 25, 26, 27, 30, 31 and 33 of IpTx$_a$ resulted in an important decrease of specific [^{3}H]ryanodine binding (Figures 4B, 4C and 4D). In particular, the R24A, R31A and R33A analogues completely abolished specific [^{3}H]ryanodine binding to RyR1. Other drastic decreases of specific [^{3}H]ryanodine binding were observed with L7A, K22A and R23A analogues (Figure 4D). In the case of acidic residues, alanine replacement resulted in slightly decreased EC_{50} values, indicating that the negatively charged residues in IpTx$_a$ slightly obstruct the ability of the toxin molecule to activate RyR1. The CD spectral analyses showed that the conformations of the alanine-scanning analogues were almost identical with that of *w*IpTx$_a$ (Figure 1), except for the single case of the linear analogue (Ala^{3,10,16,17,21,32})IpTx$_a$, which displayed completely abolished activity (Figure 4D).

Previously, Gurrola et al. [17] reported that the mutations of Arg^{23} (R23E) and Thr^{26} (T26A and T26E) in IpTx$_a$ decreased the capacity of IpTx$_a$ to activate RyR1, and suggested that in IpTx$_a$, a

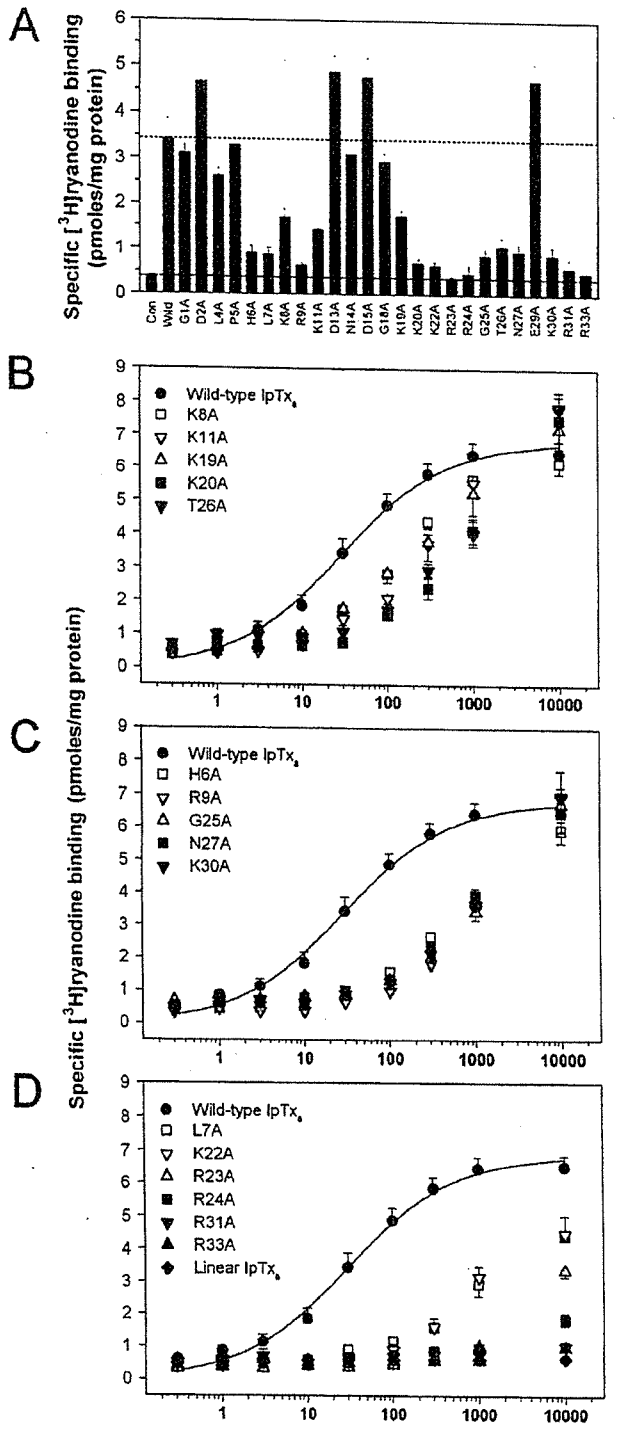

Figure 4 Activity measurements of *w*IpTx$_a$ and alanine-scanning analogues calculated with the [^{3}H]ryanodine binding assay

(**A**) Con and Wild are specific [^{3}H]ryanodine binding to RyR1 in the absence (0.38 ± 0.01 pmol/mg) and presence (3.44 ± 0.43 pmol/mg) of *w*IpTx$_a$ (30 nM) respectively. The values are the means ± S.E.M. of five independent experiments. (**B**)–(**D**) Dose-dependent activation of [^{3}H]ryanodine binding to RyR1 by *w*IpTx$_a$ and its analogues. The effect of *w*IpTx$_a$ on [^{3}H]ryanodine binding was compared with that of K8A, K11A, K19A, K20A and T26A (**B**), H6A, R9A, G25A, N27A and K30A (**C**), L7A, K22A, R23A, R24A, R31A, R33A and the linear analogue [(Ala^{3,10,16,17,21,32})IpTx$_a$] (**D**). The values are means ± S.E.M. of five independent replicates. Single-letter amino acid codes are used for the mutations.

Table 2 EC_{50} values of *w*IpTx$_a$ and analogues

The data are means ± S.E.M. of five replicated experiments (see the Materials and methods section). + and – indicate the alanine-scanning analogue of positively and negatively charged residues of IpTx$_a$ respectively.

	Analogue	EC_{50} (nM)
	Wild-type	28.40 ± 6.71
	G1A	33.40 ± 4.83
–	D2A	12.20 ± 2.17
	L4A	54.75 ± 7.79
	P5A	40.57 ± 5.18
	H6A	588.46 ± 71.24
	L7A	2769.22 ± 591.42
+	K8A	130.53 ± 15.97
+	R9A	727.58 ± 112.50
+	K11A	193.90 ± 34.72
–	D13A	9.21 ± 2.66
	N14A	32.25 ± 4.45
–	D15A	10.40 ± 1.05
	G18A	33.07 ± 5.14
+	K19A	140.97 ± 24.93
+	K20A	480.36 ± 92.21
+	K22A	1985.72 ± 383.56
+	R23A	11884.93 ± 2767.73
+	R24A	> 1 000 000
	G25A	680.52 ± 194.31
	T26A	327.12 ± 104.41
	N27A	570.52 ± 124.22
–	E29A	12.06 ± 1.30
+	K30A	615.88 ± 130.13
+	R31A	> 1 000 000
+	R33A	> 1 000 000
	Linear*	> 1 000 000

* Linear analogue [(Ala^{3,10,16,17,21,32})IpTx$_a$] was created by replacing all six cysteine residues with alanines.

cluster of basic residues (Lys^{19}–Arg^{24}) followed by Thr^{26} mimics the II–III loop of the DHPR α-subunit and is important for binding to RyR1. This agrees in part with our findings from analysis of analogues with alanine replacement of Arg^{23} and Thr^{26}. Through a series of dose-dependent experiments using a complete set of alanine-scanning analogues, however, we found that the most critical residues responsible for RyR1 activation (Arg^{24}, Arg^{31} and Arg^{33}, together with residues Lys^{22} and Arg^{23}) are located within the C-terminal region of IpTx$_a$. In addition, Leu^7 is of great importance, as it serves as a hydrophobic partner in the specific interaction with RyR1 (Figure 4D). The three-dimensional IpTx$_a$ structure shows that these six essential residues, together with other several important residues (His^6, Lys^8, Arg^9, Lys^{11}, Lys^{19}, Lys^{20}, Gly^{25}, Thr^{26}, Asn^{27} and Lys^{30}), are clustered together on one surface of the toxin molecule (an area of approx. 1900 Å^2) (Figure 5B). This region forms a functional surface with a putative binding site that probably interacts with the RyR1 cytoplasmic region. Interestingly, the opposite site is rich in acidic residues (Asp^2, Asp^{13}, Asp^{15} and Glu^{29}), and it forms a striking contrast with the positively charged functional surface (Figure 3C).

Structural comparisons with Mca and peptide A

In addition to IpTx$_a$, another exogenous ligand derived from scorpion venom mimics the effect of peptide A on RyR1. Mca, a 33-mer peptide toxin isolated from the venom of *Scorpio maurus*, activates RyR1 and shares 82 % sequence identity with IpTx$_a$ [43]. As expected from this high degree of sequence identity,

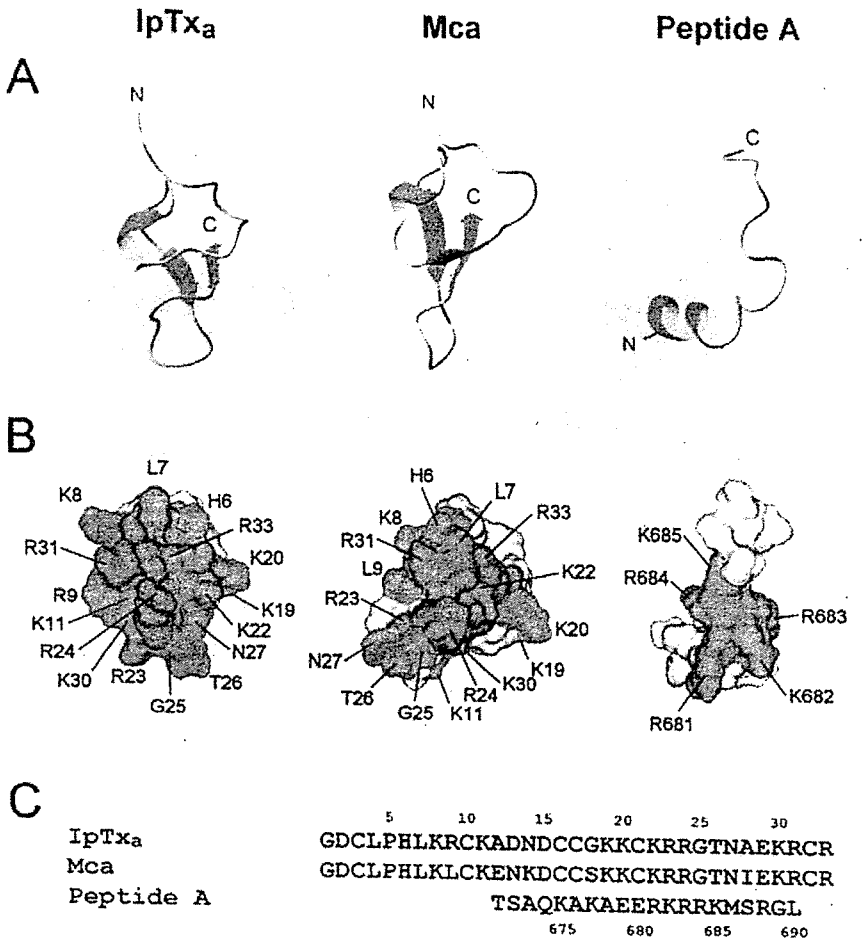

Figure 5 Structural comparison of IpTx$_a$, Mca (PDB code, 1C6W) and peptide A (PDB code, 1DU1)

(**A**) Schematic diagrams of IpTx$_a$, Mca and peptide A illustrating the location of the β-strands (cyan) and 3_{10}-helical turn (red and yellow). (**B**) Surface profiles of IpTx$_a$, Mca and peptide A. For comparison, amino acids involved in the function of these peptides are emphasized in colour. Corresponding amino acids in Mca and peptide A, six essential amino acids (L7, K22, R23, R24, R31 and R33) of IpTx$_a$ and maurocalcine, and the R681–K685 region of peptide A are shown in purple; ten functionally important residues (H6, K8, R9, K11, K19, K20, G25, T26, N27 and K30) of IpTx$_a$ and maurocalcine are shown in green. Single-letter amino acid codes are used. (**C**) Comparative arrangements of the amino acid sequences of IpTx$_a$, Mca and peptide A.

both scorpion toxins present a similar overall molecular fold in solution. Mosbah et al. [44] determined the NMR solution structure of Mca, showing that it consists of three β-strands and four chain reversals. This report suggested that the three-dimensional surface of Mca has a unique charge distribution with a marked anisotropy that emerges from the molecule through its basic surface. Such a dipole moment is also observed in the surface profile of IpTx$_a$ (Figure 3C). IpTx$_a$ is the same length as Mca, and the two differ by only six amino acid residues: those at positions 9, 12, 13, 14, 18 and 28. Except for the Arg^9 residue, all residues of IpTx$_a$ that are important to RyR1 activation are well conserved in the primary and tertiary structures of Mca (Figure 5B), enclosing a slightly decreased functional surface area of approx. 1600 Å^2. Thus it would be reasonable to expect both scorpion toxins to have a similar binding affinity for a common site on RyR1 that is important for skeletal muscle E–C coupling. However, it should be noted that these scorpion toxins have different levels of effect on RyR1 gating, which undergoes a reversible transition between subconductance and fast gating states. Although both toxins may share a binding site on RyR1, IpTx$_a$ and Mca induce subconductances that correspond to 28 % and 48 %, respectively, of the native full conductance at the positive holding potential [43,45]. This result seems to imply that a small change in the local charge distribution, due to variation of six amino acids, may induce slightly different substates in toxin gating of RyR1.

A major structural difference between IpTx$_a$ and Mca is found near the N-terminus, where Mca forms an additive peripheral β-strand (residues 9–11) that participates in the triple-stranded β-sheet (Figure 5A), but the corresponding sequence of IpTx$_a$ consists of only a single residue (Cys^{10}) that is hydrogen-bonded to the central β-strand. Interestingly, the first residue (Leu^9) of β-strand I in Mca joins with the side-chains of Cys^{10}, Cys^{16}, Cys^{21} and Cys^{32} to form the molecule's hydrophobic core. In IpTx$_a$, this residue is replaced by a positively charged arginine that plays a functional role in RyR1 activation. It is thus likely that some variations in amino acid sequences between IpTx$_a$ and Mca are to meet the structural and/or functional requirements of toxin molecules that evolve from different venomous sources.

In contrast, the solution conformation of the peptide A segment from the II–III loop of skeletal DHPR distinctly differs from that

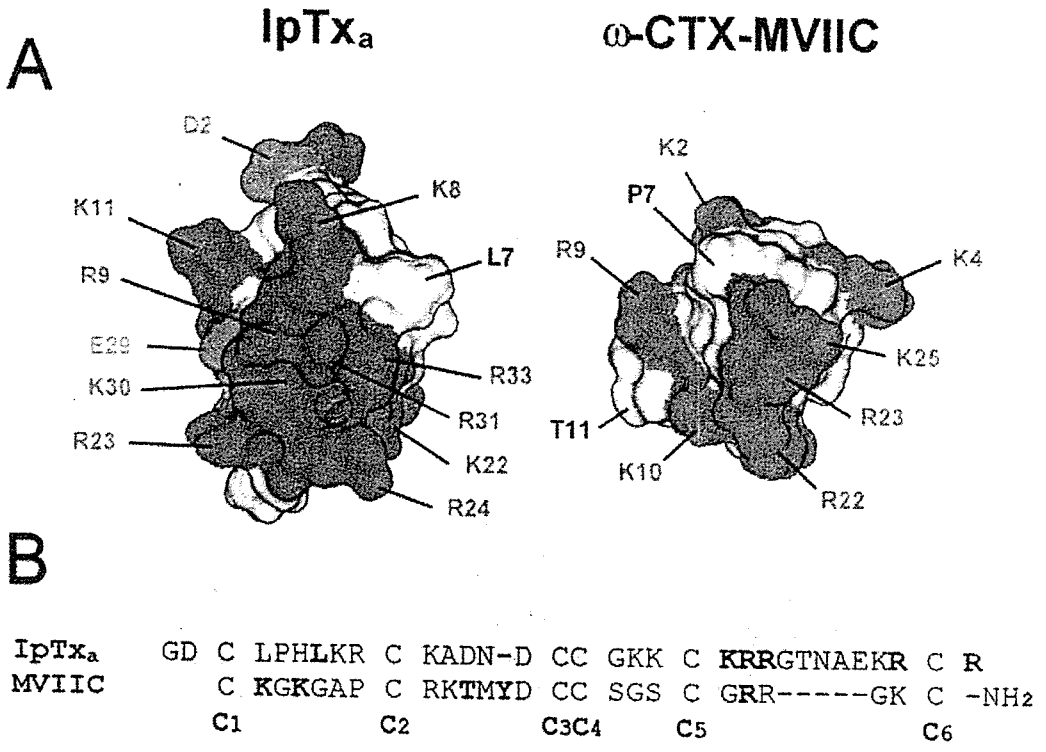

Figure 6 Structural comparison of IpTx$_a$ and ω-CTX-MVIIC

(**A**) Comparison between surface profiles of IpTx$_a$ and ω-CTX-MVIIC (PDB code 1CNN). The colour codes are the same as those in Figure 3(C). The molecules are oriented with the positively charged amino acid cluster of each molecule in a certain plane. (**B**) Amino acids in the active sites of IpTx$_a$ and MVIIC are emboldened in their primary sequence alignments.

of IpTx$_a$ [46]. As shown in Figure 5(A), the structure of peptide A consists of a helical segment extending from the N-terminus to residue Lys^{685}, which is followed by a disordered region that extends through to the C-terminus. Despite this structural difference, these peptide activators show a distinct similarity in the spatial orientation of active residues necessary to target the common binding site on RyR1. It was previously reported that the peptide A-related segment (Glu^{666}–Leu^{690}) might bind to the same site as IpTx$_a$ on RyR1 [17]. In terms of competitive binding, peptide A presents a basic surface profile with the five consecutive residues (Arg^{681}–Lys^{685}) clustered at the C-terminal end of the α-helix, whereas IpTx$_a$ presents similar positively charged residues (Lys^{22}, Arg^{23}, Arg^{24}, Arg^{31} and Arg^{33}) aligned in a central region (Figure 5B). In both peptides, these basic surfaces are fully exposed to the solvent and present a characteristic shape that may be directly involved in the RyR1 activation important for skeletal muscle E–C coupling. Together, these observations may explain, at least in part, how IpTx$_a$ and peptide A compete for a common binding site on the RyR1 channel protein.

However, although both use a common binding site, the affinities of IpTx$_a$ and peptide A for RyR1 differ. IpTx$_a$ activates RyR1 with a high nanomolar affinity, whereas peptide A activates RyR1 with a lower micromolar affinity [17]. As summarized in Table 2, the EC_{50} values for the IpTx$_a$ alanine-scanning analogues varied considerably depending on the location of the substitution. [^{3}H]Ryanodine binding to RyR1 was significantly reduced following alanine replacement of all tested basic residues, including the five critical residues (Lys^{22}, Arg^{23}, Arg^{24}, Arg^{31} and Arg^{33}), and several other residues (His^6, Leu^7, Gly^{25}, Thr^{26} and Asn^{27}), indicating that amino acid residues involved in RyR1 activation make up over the half of the toxin molecule with the exception of cysteine residues. In contrast, the functional surface of peptide A includes only five consecutive basic residues (Arg^{681}, Lys^{682}, Arg^{683}, Arg^{684} and Lys^{685}) that are clustered at the C-terminal end of the α-helix. In three dimensions, IpTx$_a$ exhibits a large functional surface area, approx. 1900 Å^2, whereas peptide A bears a much smaller functional surface area, approx. 800 Å^2.

In measurements of single channel currents, IpTx$_a$ induced a long-lived subconductance state in RyR1 that possessed 28 % of the characteristic full open state at the positive holding potential. In contrast, peptide A induced long-lived channel closures with occasional burst transitions to subconductance states of 65 % or 86 % of the full conductance, indicating that IpTx$_a$ and peptide A stabilize distinct RyR1 gating states through somewhat different interaction mechanisms [47].

Overall, these results suggest that the site where peptide A binds to RyR1 belongs to a subset of macrosites capable of being occupied by IpTx$_a$, resulting in differing the affinity and the mode of activation.

Structural comparison with ω-CTX-MVIIC, a voltage-gated P/Q-type Ca^{2+} channel blocker

Voltage-gated Ca^{2+} channels are classified into several subtypes, which include the L-, N-, P-, Q-, R- and T-subtypes, according to their electrophysiological and pharmacological properties [48]. ω-CTXs are highly potent blockers of voltage-gated Ca^{2+} channels and are useful ligands for the pharmacological discrimination of Ca^{2+} channel subtypes [49]. Extensive structure–activity

studies have revealed that all ω-CTXs (e.g. ω-CTX-GVIA and -MVIIA, N-type Ca^{2+}-channel blockers, and the ω-CTX-MVIIC, P/Q-type Ca^{2+}-channel blocker) share significant structural similarity in three dimensions, but possess distinct functional sites responsible for the specific interaction with individual voltage-gated Ca^{2+} channel subtypes [50–53]. The molecular architecture of the cone-snail ω-CTXs is entirely composed of an 'inhibitor cystine knot' fold constrained by three intramolecular disulphide bonds. This structure is also found in the RyR1-targeting scorpion toxins $IpTx_a$ and Mca, indicating that the ω-scaffold is a general molecular topology of exogenous toxins targeting the Ca^{2+} channels.

Among ω-CTXs, ω-CTX-MVIIC is the most structurally similar to the scorpion RyR1 activators. As shown in Figure 6(A), ω-CTX-MVIIC exhibits a highly basic structural surface that includes several positively charged amino acid residues. Although there is a high degree of structural similarity between $IpTx_a$ and ω-CTX-MVIIC, the two Ca^{2+}-channel-targeting toxins show no cross-reactivity; $IpTx_a$ has no affinity for the P/Q-type Ca^{2+} channel and ω-CTX-MVIIC has no affinity for the RyR1 [17]. This suggests that the two toxins form distinct functional sites responsible for the specific interaction with each channel protein [53]. The functionally important residues of $IpTx_a$ for the binding to RyR1 consist of five protruding basic residues (Lys^{22}, Arg^{23}, Arg^{24}, Arg^{31} and Arg^{33}) and one hydrophobic residue (Leu^7), with approx. ten additional residues assisting. In contrast, the functional residues for ω-CTX-MVIIC action on the P/Q-type Ca^{2+} channel include three basic residues (Lys^2, Lys^4 and Arg^{22}) and two polar residues (Thr^{11} and Tyr^{13}) [53], suggesting that $IpTx_a$ forms a larger functional surface than does ω-CTX-MVIIC. ω-CTX-MVIIC is shorter in length than $IpTx_a$, and its positively charged surface area is also smaller than that of $IpTx_a$, mainly due to fewer basic amino acids between the fifth cysteine and the C-terminus (three compared with six) (Figure 6B). In $IpTx_a$, this region forms a long hairpin loop with an electropositive potential, incorporating β-strands I and II (Figure 3B). As previously mentioned, both $IpTx_a$ and peptide A share a necessary alignment of five basic residues that act at a common site on RyR1 (Figure 5B). ω-CTX-MVIIC also possesses a similar basic structural region, consisting of five basic residues (Arg^9, Lys^{10}, Arg^{22}, Arg^{23} and Lys^{25}) (Figure 6A), but its shape is relatively different from that of both $IpTx_a$ and peptide A, resulting in a failure to activate RyR1. Taken together, these observations suggest that the correct distribution of surface charges is important to specific interaction with RyR1, rather than the globular structure maintained by the conserved disulphide framework. This may be one reason why ω-CTX-MVIIC does not compete for the same binding site as $IpTx_a$ and peptide A, thus providing structural and molecular insights into the specific interaction mode of RyR1-targeting peptide effectors.

Conclusion

In the present study, we have determined the NMR solution structure of the peptide activator $IpTx_a$, and identified the functional surface that is responsible for its high-affinity interaction with RyR1. A detailed comparison between $IpTx_a$ and peptide A revealed that the existence of complementary surface profiles, created by different molecular scaffolds, is limited between the C-terminal β-sheet region of $IpTx_a$ and the α-helical end region of peptide A. Thus it seems that the site where peptide A binds to RyR1 belongs to a subset of the macrosites occupied by $IpTx_a$, resulting in differing affinities and subconductance states. A comparative surface analysis with ω-CTX-MVIIC suggests that the characteristic shape of positively charged binding surface rather than globular shape is responsible for the specific interaction of RyR1-targeting peptide effectors. Taken together, these structural and functional studies on ryanodine-sensitive channel effectors, together with our knowledge of the three-dimensional structure of DHPR and RyR1 obtained previously by cryo-electron microscopy and image processes [54,55], open up a new avenue for the elucidation of the molecular details of skeletal type E–C coupling.

This study was supported by grants from the Korean Ministry of Science and Technology (Critical Technology 21, 00-J-LF-01-B-54), the Korea Science and Engineering Foundation through the Research Center for Proteineous Materials (The Ministry of Science and Technology). C. W. L. and E. H. L. are supported in part by the Korean Ministry of Education (Brain Korea 21 programme).

REFERENCES

1 Bers, D. M. (1991) Excitation–Contraction Coupling and Cardiac Contractile Force, Kluwer Academic Publishers, Dordrecht
2 Nabauer, M., Callewaert, G., Cleemann, L. and Morad, M. (1989) Regulation of calcium release is gated by calcium current, not gating charge, in cardiac myocytes. Science **244**, 800–803
3 Armstrong, C. M., Bezanila, F. M. and Horowicz, P. (1972) Twitches in the presence of ethylene glycol bis(-aminoethyl ether)-N,N'-tetracetic acid. Biochim. Biophys. Acta **267**, 605–608
4 Marty, I., Robert, M., Villaz, M., De Jongh, K. S., Lai, Y., Catterall, W. A. and Ronjat, M. (1994) Biochemical evidence for a complex involving dihydropyridine receptor and ryanodine receptor in triad junctions of skeletal muscle. Proc. Natl. Acad. Sci. U.S.A. **91**, 2270–2274
5 Tanabe, T., Beam, K. G., Adams, B. A., Niidome, T. and Numa, S. (1990) Regions of the skeletal muscle dihydropyridine receptor critical for excitation–contraction coupling. Nature (London) **346**, 567–569
6 Lu, X., Xu, L. and Meissner, G. (1994) Activation of the skeletal muscle calcium release channel by a cytoplasmic loop of the dihydropyridine receptor. J. Biol. Chem. **269**, 6511–6516
7 El-Hayek, R., Antoniu, B., Wang, J., Hamilton, S. L. and Ikemoto, N. (1995) Identification of calcium release-triggering and blocking regions of the II–III loop of the skeletal muscle dihydropyridine receptor. J. Biol. Chem. **270**, 22116–22118
8 Nakai, J., Dirksen, R. T., Nguyen, H. T., Pessah, I. N., Beam, K. G. and Allen, P. D. (1996) Enhanced dihydropyridine receptor channel activity in the presence of ryanodine receptor. Nature (London) **380**, 72–75
9 Slavik, K. J., Wang, J. P., Aghdasi, B., Zhang, J. Z., Mandel, F., Malouf, N. and Hamilton, S. L. (1997) A carboxy-terminal peptide of the α1-subunit of the dihydropyridine receptor inhibits Ca^{2+} release channels. Am. J. Physiol. **272**, C1475–C1481
10 Leong, P. and MacLennan, D. H. (1998) The cytoplasmic loops between domains II and III and domains III and IV in the skeletal muscle dihydropyridine receptor bind to a contiguous site in the skeletal muscle ryanodine receptors. J. Biol. Chem. **273**, 29958–29964
11 Grabner, M., Dirksen, R. T., Suda, N. and Beam, K. G. (1999) The II–III loop of the skeletal muscle dihydropyridine receptor is responsible for the bi-directional coupling with the ryanodine receptor. J. Biol. Chem. **274**, 21913–21919
12 Sencer, S., Papineni, R. V., Halling, D. B., Pate, P., Krol, J., Zhang, J. Z. and Hamilton, S. L. (2001) Coupling of RYR1 and L-type calcium channels via calmodulin binding domains. J. Biol. Chem. **276**, 38237–38241
13 Nakai, J., Sekiguchi, N., Rando, T. A., Allen, P. D. and Beam, K. G. (1998) Two regions of the ryanodine receptor involved in coupling with L-type Ca^{2+} channels. J. Biol. Chem. **273**, 13403–13406
14 El-Hayek, R., Lokuta, A. J., Arevalo, C. and Valdivia, H. H. (1995) Peptide probe of ryanodine receptor function. J. Biol. Chem. **270**, 28696–28704
15 Zamudio, F. Z., Gurrola, G. B., Arevalo, C., Sreekumar, R., Walker, J. W., Valdivia, H. H. and Possani, L. D. (1997) Primary structure and synthesis of Imperatoxin A ($IpTx_a$), a peptide activator of Ca^{2+} release channels/ryanodine receptors. FEBS Lett. **405**, 385–389
16 El-Hayek, R. and Ikemoto, N. (1998) Identification of the minimum essential region in the II–III loop of the dihydropyridine receptor 1 subunit required for activation of skeletal muscle-type excitation–contraction coupling. Biochemistry **37**, 7015–7020
17 Gurrola, G. B., Arevalo, C., Sreekuma, R., Lokuta, A. J., Walker, J. W. and Valdivia, H. H. (1999) Activation of ryanodine receptors by imperatoxin A and a peptide segment of the II–III loop of the dihydropyridine receptor. J. Biol. Chem. **274**, 7879–7886

18 Green, D., Pace, S., Curtis, S. M., Sakowska, M., Lamb. G. D., Dulhunty, A. F. and Casarotto, M. G. (2003) The three-dimensional structural surface of two β-sheet scorpion toxins mimics that of an α-helical dihydropyridine receptor segment. Biochem. J. **370**, 517–527
19 Rance, M., Sørensen, O. W., Bodenhausen, G., Wagner, G., Ernst, R. R. and Wüthrich, K. (1983) Improved spectral resolution in COSY ^{1}H NMR spectra of protein via double quantum filtering. Biochem. Biophys. Res. Commun. **117**, 479–485
20 Griesinger, C., Sørensen, O. W. and Ernst, R. R. (1987) Practical aspects of the E.COSY technique: measurement of scalar spin–spin coupling constants in peptides. J. Magn. Reson. **75**, 474–492
21 Bax, A. and Davis, D. G. (1985) MLEV-17-based two-dimensional homonuclear magnetization transfer spectroscopy. J. Magn. Reson. **65**, 355–360
22 Jeener, J., Meier, B. N., Bachmann, P. and Ernst, R. P. (1979) Investigation of exchange processes by two-dimensional NMR spectroscopy. J. Chem. Phys. **71**, 4546–4553
23 Wüthrich, K., Billeter, M. and Braun, W. (1983) Pseudo-structures for the 20 common amino acids for use in studies of protein conformations by measurement of intramolecular proton–proton distance constraints with nuclear magnetic resonance. J. Mol. Biol. **169**, 949–961
24 Clore, M., Gronenborn, A. M., Nilges, M. and Ryan, C. A. (1987) Three-dimensional structure of potato carboxypeptidase inhibitor in solution: a study using nuclear magnetic resonance, distance geometry and restraint molecular dynamics. Biochemistry **26**, 8012–8023
25 Nilges, M., Gronenborn, A. M., Brünger, A. T. and Clore, G. M. (1988) Determination of three-dimensional structures of proteins by simulated annealing with interproton distance restraints: application to crambin, potato carboxypeptidase inhibitor and barley serine proteinase inhibitor 2. Protein Eng. **2**, 27–38
26 Brünger, A. T. (1993) X-PLOR Manual, Version 3.1, Yale University, New Haven
27 Laskowski, R. A., Rullmann, J. A., MacArthur, M. W., Kaptein, R. and Thornton, J. M. (1996) AQUA and PROCHECK-NMR: programs for checking the quality of protein structures solved by NMR. J. Biomol. NMR **8**, 477–486
28 Hutchinson, E. G. and Thornton, J. M. (1996) PROMOTIF – a program to identify and analyze structural motifs in proteins. Protein Sci. **5**, 212–220
29 Koradi, R., Billeter, M. and Wüthrich, K. (1996) MOLMOL: a program for display and analysis of macromolecular structures. J. Mol. Graph. **14**, 29–32
30 Kim, D. H., Sreter, F. A., Ohnishi, S. T., Ryan, J. F., Roberts, J., Allen, P. D., Meszaros, L. G., Antonia, B. and Ikemoto, N. (1984) Kinetic studies of Ca^{2+} release from sarcoplasmic reticulum of normal and malignant hyperthermia susceptible pig muscles. Biochim. Biophys. Acta **775**, 320–327
30a Bradford, M. M. (1976) A rapid and sensitive method for the quantitation of microgram quantities of protein utilizing the principle of protein-dye binding. Anal. Biochem. **72**, 248–254
31 Campbell, K. P., Knudson, C. M., Imagawa, T., Leung, A. T., Sutko, J. L., Kahl, S. D., Raab, C. R. and Madson, L. (1987) Identification and characterization of the high affinity [^{3}H]ryanodine receptor of the junctional sarcoplasmic reticulum Ca^{2+} release channel. J. Biol. Chem. **262**, 6460–6463
32 Kim, D. H., Mkparu, F., Kim, C. R. and Caroli, R. F. (1994) Alteration of Ca^{2+} release channel function in sarcoplasmic reticulum of pressure-overload-induced hypertrophic rat heart. J. Mol. Cell. Cardiol. **26**, 1505–1512
33 Wüthrich, K. (1986). NMR of Proteins and Nucleic Acids, John Wiley and Sons, Inc., New York
34 Pallaghy, P. K., Nielsen, K. J., Craik, D. J. and Norton, R. S. (1994) A common structural motif incorporating a cystine knot and a triple-stranded β-sheet in toxic and inhibitory polypeptides. Protein Sci. **3**, 1833–1839
35 Norton, R. S. and Pallaghy, P. K. (1998) The cystine knot structure of ion channel toxins and related polypeptides. Toxicon **36**, 1573–1583
36 Davis, J. H., Bradley, E. K., Miljanich, G. P., Nadasdi, L., Ramachandran, J. and Basus, V. J. (1993) Solution structure of omega-conotoxin GVIA using 2-D NMR spectroscopy and relaxation matrix analysis. Biochemistry **32**, 7396–7405
37 Pallaghy, P. K., Duggan, B. M., Pennington, M. W. and Norton, R. S. (1993) Three-dimensional structure in solution of the calcium channel blocker ω-conotoxin. J. Mol. Biol. **234**, 405–420
38 Kohno, T., Kim, J. I., Kobayashi, K., Kodera, Y., Maeda, T. and Sato, K. (1995) Three-dimensional structure in solution of the calcium channel blocker ω-conotoxin MVIIA. Biochemistry **34**, 10256–10265
39 Kim, J. I., Konishi, S., Iwai, H., Kohno, T., Gouda, H., Shimada, I., Sato, K. and Arata, Y. (1995) Three-dimensional solution structure of the calcium channel antagonist ω-agatoxin IVA: consensus molecular folding of calcium channel blockers. J. Mol. Biol. **250**, 659–671
40 Reily, M. D., Thanabal, V. and Adams, M. E. (1995) The solution structure of ω-Aga-IVB, a P-type calcium channel antagonist from venom of the funnel web spider, *Agelenopsis aperta*. J. Biomol. NMR **5**, 122–132
41 Saether, O., Craik, D. J., Campbell, I. D., Sletten, K., Juul, J. and Morman, D. G. (1995) Elucidation of the primary and three-dimensional structure of the uterotonic polypeptide kalata B1. Biochemistry **34**, 4147–4158
42 Nilges, M., Habazettl, J., Brünger, A. T. and Holak, T. A. (1991) Relaxation matrix refinement of the solution structure of squash trypsin inhibitor. J. Mol. Biol. **248**, 106–124
43 Fajloun, Z., Kharrat, R., Chen, L., Lecomte, C., Di Luccio, E., Bichet, D., El Ayeb, M., Rochat, H., Allen, P. D., Pessah, I. N. et al. (2000) Chemical synthesis and characterization of maurocalcine, a scorpion toxin that activates Ca^{2+} release channel/ryanodine receptors. FEBS Lett. **469**, 179–185
44 Mosbah, A., Kharrat, R., Fajloun, Z., Renisio, J. G., Blanc, E., Sabatier, J. M., El Ayeb, M. and Darbon, H. (2000) A new fold in the scorpion toxin family, associated with an activity on a ryanodine-sensitive calcium channel. Proteins **40**, 436–442
45 Tripathy, A., Resch, W., Xu, L., Valdivia, H. H. and Meissner, G. (1998) Imperatoxin A induces subconductance states in Ca^{2+} release channels (ryanodine receptors) of cardiac and skeletal muscle. J. Gen. Physiol. **111**, 679–690
46 Casarotto, M. G., Gibson, F., Pace, S. M., Curtis, S. M., Mulcair, M. and Dulhunty, A. F. (2000) A structural requirement for activation of skeletal ryanodine receptors by peptides of the dihydropyridine receptor II–III loop. J. Biol. Chem. **275**, 11631–11637
47 Chen, L., Esteve, E., Sabatier, J. M., Ronjat, M., Waard, M. D., Allen, P. D. and Pessah, I. N. (2003) Maurocalcine and peptide A stabilize distinct subconductance states of ryanodine receptor type 1 (RyR1) revealing a proportional gating mechanism. J. Biol. Chem. **278**, 16095–16106
48 Snutch, T. P. and Reiner, P. B. (1992) Ca^{2+} channels: diversity of form and function. Curr. Opin. Neurobiol. **2**, 247–253
49 Olivera, B. M., Miljanich, G. P., Ramachandran, J. and Adams, M. E. (1994) Calcium channel diversity and neurotransmitter release: the ω-conotoxins and ω-agatoxins. Annu. Rev. Biochem. **63**, 823–867
50 Kim, J. I., Takahashi, M., Ogura, A., Kohno, T., Kudo, Y. and Sato, K. (1994) Hydroxyl group of Tyr^{13} is essential for the activity of ω-conotoxin GVIA, a peptide toxin for N-type calcium channel. J. Biol. Chem. **269**, 23876–23878
51 Kim, J. I., Takahashi, M., Ohtake, A., Wakamiya, A. and Sato, K. (1995) Tyr^{13} is essential for the activity of ω-conotoxin MVIIA and GVIA, specific N-type calcium channel blockers. Biochem. Biophys. Res. Commun. **206**, 449–454
52 Kim, J. I., Takahashi, M., Martin-Moutot, N., Seagar, M. J., Ohtake, A. and Sato, K. (1995) Tyr^{13} is essential for the binding of ω-conotoxin MVIIC to the P/Q-type calcium channel. Biochem. Biophys. Res. Commun. **214**, 305–309
53 Sato, K., Raymond, C., Martin-Moutot, N., Sasaki, T., Ohtake, A., Minami, K., Van Renterghem, C., Kim, J. I., Takahashi, M. and Seagar, M. J. (2000) Binding of Ala-scanning analogs of ω-conotoxin MVIIC to N- and P/Q-type calcium channels. FEBS Lett. **469**, 147–150
54 Samso, M., Trujillo, R., Gurrola, G. B., Valdivia, H. H. and Wagenknecht, T. (1999) Three-dimensional location of the imperatoxin A binding site on the ryanodine receptor. J. Cell Biol. **146**, 493–499
55 Serysheva, I. I., Ludtke, S. J., Baker, M. R., Chiu, W. and Hamilton, S. L. (2002) Structure of the voltage-gated L-type Ca^{2+} channel by electron cryomicroscopy. Proc. Natl. Acad. Sci. U.S.A. **99**, 10370–10375
56 Brooks, B. R., Bruccoleri, R. E., Olafson, B. D., States, D. J., Swaminathan, S. and Karplus, M. (1983) CHARMm: a program for macromolecular energy, minimization, and dynamics calculations. J. Comput. Chem. **4**, 187–217

Received 7 August 2003/29 September 2003; accepted 9 October 2003
Published as BJ Immediate Publication 9 October 2003, DOI 10.1042/BJ20031192

Available online at www.sciencedirect.com

SCIENCE DIRECT

European Journal of Pharmacology 499 (2004) 265–274

ejp

www.elsevier.com/locate/ejphar

Adenosine A_1-receptor-mediated tonic inhibition of glutamate release at rat hippocampal CA3–CA1 synapses is primarily due to inhibition of N-type Ca^{2+} channels

Satoshi Manita[a], Yoshinobu Kawamura[a], Kazuki Sato[b], Masashi Inoue[a], Yoshihisa Kudo[a], Hiroyoshi Miyakawa[a,*]

[a]*Laboratory of Cellular Neurobiology, School of Life Science, Tokyo University of Pharmacy and Life Science, Hachioji, Tokyo 192-0392, Japan*
[b]*Faculty of Human Environmental Science, Fukuoka Women's University, Kasumigaoka, Higashi-ku, Fukuoka 813-8529, Japan*

Received 11 March 2004; received in revised form 28 July 2004; accepted 30 July 2004

Abstract

The voltage-gated Ca^{2+} channels responsible for synaptic transmission at CA3–CA1 synapses are mainly P/Q- and N-types. It has been shown that tonic inhibition of transmission due to activation of adenosine A_1 receptors occurs at this synapse. We have recently developed a technique to monitor synaptically released glutamate which is based on synaptically induced glial depolarisation. Using this technique, we have examined the effects of different voltage-gated Ca^{2+} channel blockers on glutamate release. Under conditions in which the adenosine A_1 receptor was not blocked, ω-AgaIVA (a P/Q-type voltage-gated Ca^{2+} channel blocker) suppressed synaptically induced glial depolarisation to a greater extent than ω-CgTxGVIA (an N-type voltage-gated Ca^{2+} channel blocker) did. In contrast, in the presence of an adenosine A_1 receptor antagonist, ω-AgaIVA was less effective at suppressing synaptically induced glial depolarisation than ω-CgTxGVIA. These results indicate that, in the absence of adenosine A_1 receptor-mediated tonic inhibition, the contribution of N-type is much greater than that of P-type, and that N-types are the primary target of tonic inhibition in normal conditions in which adenosine A_1 receptor-mediated tonic inhibition is present.

Keywords: Presynaptic terminal; Ca^{2+} channel; Adenosine receptor; Hippocampus

1. Introduction

Transmitter release at presynaptic terminals is one of the major targets for neuromodulation (Vizi, 2000). For example, it has been shown that activation of presynaptic receptors, such as metabotropic glutamate (Cartmell and Schoepp, 2000), adenosine A_1 (Dunwiddie and Masino, 2001), gamma-aminobutyric acid $(GABA)_B$ (Misgeld et al., 1995) and muscarinic and cannabinoid (Schlicker and Kathmann, 2001) receptors, modulates transmitter release at hippocampal CA3–CA1 synapses, and that inhibition of voltage-gated Ca^{2+} channels in the presynaptic terminals can be responsible for this modulation (Ambrosio et al., 1997; Mogul et al., 1993; Wu and Saggau, 1997).

Various studies have shown that N- and P/Q-type channels are responsible for glutamate release at CA3–CA1 synapses in the rat hippocampus (Luebke et al., 1993; Takahashi and Momiyama, 1993; Wheeler et al., 1994; Wu and Saggau, 1994b, 1997; Reuter, 1995; Reuter, 1996). Measuring Ca^{2+}-dependent [^{3}H]glutamate release from hippocampal synaptosomes using biochemical techniques, Luebke et al. (1993) reported that P-type channels play a more prominent role than N-type channels. Takahashi and Momiyama (1993) showed that excitatory postsynaptic currents in hippocampal CA1 neurons in slice preparations are suppressed to a greater extent by ω-AgaIVA, a P-type channel blocker, than by ω-CgTxGVIA, an N-type channel

* Corresponding author. Tel.: +81 426 76 7183; fax: +81 426 76 8841.
E-mail address: miyakawa@ls.toyaku.ac.jp (H. Miyakawa).

0014-2999/$ - see front matter © 2004 Elsevier B.V. All rights reserved.
doi:10.1016/j.ejphar.2004.07.113

blocker (84% and 31% suppression, respectively). This finding was confirmed by Wheeler et al. (1994), who showed that the slope of the field excitatory post synaptic potential (fEPSP) at synapses from CA3 to CA1 pyramidal neurons in the hippocampus is reduced by ω-AgaIVA to a greater extent than by ω-CgTxGVIA (85% and 46%, respectively). Wu and Saggau (1994b) performed fast Ca^{2+} imaging of presynaptic terminals at rat CA3–CA1 synapses and reported that application of N- or P/Q-type channel blockers reduces presynaptic Ca^{2+} influxes by 21% or 35%, respectively. These studies showed that the contribution of P/Q-type channels is greater than that of N-type channels. In contrast, Reuter (1995) reported that, in rat hippocampal cell cultures, the exocytosis of the styryl dye, FM1-43, from synaptic vesicles during synaptic transmission following Ca^{2+} entry through Ca^{2+} channels is inhibited by ω-CgTxGVIA to a greater extent than by ω-AgaIVA.

However, most of the above studies were performed under conditions in which glutamate release from presynaptic terminals might have been suppressed by the action of various modulators. For example, Wu and Saggau (1994a) reported that the adenosine A_1 antagonist, 8-cyclopentyl-1,3-dipropylxanthine (8-CPT), enhances both the presynaptic Ca^{2+} rise and the fEPSP, suggesting tonic inhibition by endogenous adenosine. It has been reported that adenosine suppress transmitter release by inhibiting voltage-gated Ca^{2+} channels (Dunwiddie and Masino, 2001). In order to determine which types of voltage-gated Ca^{2+} channels are responsible for transmitter release, it is necessary to compare contribution of voltage-gated Ca^{2+} channels in the absence of tonic inhibition.

Several different methods, such as the measurement of postsynaptic responses and presynaptic $[Ca^{2+}]_i$ changes, have been used to investigate the contribution of voltage-gated Ca^{2+} channels to transmitter release. However, these methods are rather indirect, as voltage-gated Ca^{2+} channels may be involved in determining postsynaptic responses and as there may be presynaptic $[Ca^{2+}]_i$ changes that do not contribute to transmitter release. We have recently developed a novel optical method to monitor synaptically induced glutamate release which involves detecting the depolarisation of glial cells caused by glutamate uptake using a voltage-sensitive dye and a fast optical imaging system (Kojima et al., 1999). In the present study, we monitored glutamate release at CA3–CA1 synapses in rat hippocampal slice preparations by using this method in the absence of adenosine-mediated tonic inhibition and examined the effects of specific blockers of N- and P/Q-type channels. We have confirmed that glutamate release is tonically inhibited by activation of adenosine A_1 receptors and demonstrated that, in the absence of inhibition, the contribution of N-type channels is greater than that of P/Q-type channels. Thus, N-type channels are the major target of the adenosine A_1 receptor-mediated inhibitory effect on transmission at CA3–CA1 synapses.

2. Materials and methods

The experimental protocols were approved by the Institutional Animal Care and Use Committee of the Tokyo University of Pharmacy and Life Science, and were carried out in accordance with the National Institute of Health Guide for the Care and Use of Laboratory Animals.

2.1. Slice preparation

Hippocampal slices were prepared from 3-week-old male Wistar rats. The animals were decapitated under deep diethyl ether anaesthesia, and the brains removed and rapidly cooled in artificial cerebrospinal fluid [composition (in mM): 110 choline chloride for preparing slices or 124 NaCl for experiments, 2.5 KCl, 26 $NaHCO_3$, 10 glucose, 1.25 NaH_2PO_4, 2 $CaCl_2$ and 1 $MgCl_2$, pH 7.4] bubbled continuously with a gas mixture of 95% O_2 and 5% CO_2. Slices (400 μm thick) were prepared using a rotary slicer (Dosaka EM model DTY-7700, Japan).

2.2. Voltage-sensitive dye measurement

The method has been described in detail elsewhere (Kojima et al., 1999). Briefly, slices were maintained in a holding chamber for at least 30 min, then stained with the voltage-sensitive dye, RH155 (NK3041) (Molecular Probes, Eugene, OR, or Nippon Kankoh-Shikiso, Okayama, Japan) by submersion for 30 min in artificial cerebrospinal fluid containing 0.21 mg/ml of RH155. The stained slices were placed in an experimental chamber mounted on an inverted microscope (TMD-300, Nikon, Tokyo, Japan) and changes in dye absorption, which are related to the change in membrane potential, were measured at 700 nm using a high-speed (maximum frame rate 2 kHz) 16×16 photodiode array system (Agrus-50/PDA, Hamamatsu Photonics, Hamamatsu, Japan). The photo-currents generated at the photodiodes were converted to voltage using a current-to-voltage converter with a 50 MΩ feedback resistor and the data transferred to a sample-and-hold device, then DC-coupled to a 16 bit resolution analogue-to-digital converter. All optical signals were displayed as changes in light intensity divided by the total light intensity ($\Delta I/I$). In most experiments, a ×10 objective lens (NA 0.45) was used; in this case, each diode imaged an area of 52.5×52.5 μm. Experiments were performed at 24–28 °C. Synaptic responses were evoked by delivering a short current pulse of 200 μs duration using a bipolar tungsten electrode placed in the stratum radiatum to stimulate Schaffer collaterals. The stimulus was applied every 5 s and the optical signals averaged over 9–12 trials. To record extracellular field potentials, glass pipettes (1.5×90 mm, 1–5 MΩ) filled with artificial cerebrospinal fluid were inserted into the stratum radiatum. The potentials were amplified by a high-gain AC amplifier (MEZ-8201, Nihon-Koden, Tokyo, Japan), digi-

tised, and recorded on a computer (SD-512, EPSON, Japan). The field potential responses were averaged over five trials.

2.3. Drugs

6-Cyano-7-nitroquinoxaline-2,3-dione (CNQX; a non-*N*-methyl-D-aspartate (NMDA) glutamate receptor antagonist), DL-2-amino-5-phosphonopentanoic acid (APV; an NMDA receptor antagonist), 8-cyclopentyl-1,3-dimethylxanthine (8-CPT; an adenosine A_1 receptor antagonist) and 2-chloro-N^6-cyclopentyladenosine (CCPA; an adenosine A_1 receptor agonist) were purchased from Sigma-Aldrich (Tokyo, Japan). 2-Carboxy-4-isopropyl-3-pyrrolidineacetic acid (DHK; a glial glutamate transporter antagonist) was purchased from Tocris Cookson (Bristol, UK). ω-AgaIVA and ω-CgTxGVIA were synthesized as described previously (Kim et al., 1994, 1995).

3. Results

3.1. Tonic inhibition of glutamate release at CA3–CA1 synapses by adenosine A_1 receptors

We have previously shown that glial glutamate transporter activity can be measured in the CA1 region of the hippocampus using an optical imaging technique (Kojima et al., 1999, Kawamura et al., 2004). Briefly, in normal artificial cerebrospinal fluid, the synaptically induced signals recorded from slices stained with the voltage-sensitive dye, RH155, consist of several components, including those due to presynaptic fibre volley, EPSPs and action potentials (Fig. 1A and B). In the presence of ionotropic glutamate receptor blockers, the signals due to EPSPs and action potentials disappear, leaving a slowly depolarising response that can be blocked by glutamate transporter blockers, such as DHK (Fig. 1B), and which is due to the depolarisation of astrocytes caused by the electrogenic activity of the GLT-1 glutamate transporter, which is stimulated by release of glutamate from the synapses. We therefore refer to this signal as synaptically induced glial depolarisation. The amplitude of the synaptically induced glial depolarisation signal is monotonically related to the intensity of stimulation (Fig. 1C–E).

In the present study, we examined whether application of an adenosine A_1 receptor antagonist substantially enhanced the synaptically induced glial depolarisation signal. Fig. 1C and D shows the effect of 0.5 μM 8-CPT on the synaptically induced glial depolarisation and field potential at three different stimulus intensities. In Fig. 1C and E1, the area of the synaptically induced glial depolarisation signal (0–120 ms) evoked by 0.1 or 0.3 mA was increased by 99.8% (n=5) and 150% (n=5), respectively. When the effect of 0.5 μM 8-CPT on the slope of the fEPSP was tested on a separate set of slice preparations (Fig. 1D), the slope of the fEPSPs evoked by 0.05, 0.1 and 0.3 mA was increased by 216% (n=5), 105% (n=5) and 75% (n=5), respectively (Fig. 1E2).

To confirm that the effect of 8-CPT was really due to inhibition of the adenosine A_1 receptor, we examined the effect of 8-CPT on the inhibition induced by an adenosine A_1 receptor agonist and on control transmission. Bath application of the specific adenosine A_1 receptor agonist, CCPA (0.5 μM), reduced both the amplitude of the synaptically induced glial depolarisation (Fig. 2A) and the slope of the fEPSP (Fig. 2B) to 60±9.2% (n=6) and 31±12% (n=4) of control levels, respectively. Using a combination of 0.5 μM 8-CPT and 0.5 μM CCPA, the amplitude of the synaptically induced glial depolarisation and the slope of fEPSP returned not to the basal level, but to a much higher level, the amplitude of the synaptically induced glial depolarisation reaching 226±32% (n=6) and the slope of the fEPSP 145±41% (n=4) of control levels (Fig. 2A and B). The values for the amplitude of the synaptically induced glial depolarisation and the slope of the fEPSP in the presence of 8-CPT alone were not significantly different (synaptically induced glial depolarisation p=0.34; fEPSP p=0.21 paired t-test) from those in the presence of both CCPA and 8-CPT (Fig. 2C1 and C2). Fig. 3 shows the dose dependency of the effect of 8-CPT on the amplitude of the synaptically induced glial depolarisation. The EC_{50} value was 0.9±1.1 μM.

The synaptically induced glial depolarisation signals showed a paired-pulse facilitation for a paired pulse with a 50-ms inter-pulse interval, as did the field EPSPs (Figs. 1C and 2A). Interestingly, in contrast to the paired-pulse ratio for the slope of fEPSP, the paired-pulse ratio for the synaptically induced glial depolarisation was not significantly affected by the presence of CCPA or of 8-CPT (Fig. 2D).

These results confirm those of a previous report (Wu and Saggau, 1994a), which showed that synaptic transmission at CA3–CA1 synapses is tonically inhibited by activation of adenosine A_1 receptors. We also tested whether transmission was tonically inhibited by metabotropic glutamate receptors, but found that metabotropic glutamate receptor antagonists, such as (*RS*)-α-Methyl-4-phosphonophenylglycine (MPPG), had no significant effect on the amplitude of the synaptically induced glial depolarisation (data not shown).

3.2. Adenosine A_1 receptors control glutamate release by inhibiting N-type voltage-gated Ca^{2+} channels

To examine which voltage-gated Ca^{2+} channels were responsible for transmitter release and to understand the mechanisms by which adenosine A_1 receptors inhibit synaptic transmission, we compared the effects of blockers of P/Q- and N-type voltage-gated Ca^{2+} channels on the amplitude of the synaptically induced glial depolarisation in the presence and absence of 8-CPT. To block adenosine A_1 receptor-mediated inhibition, 10 μM 8-CPT was applied to

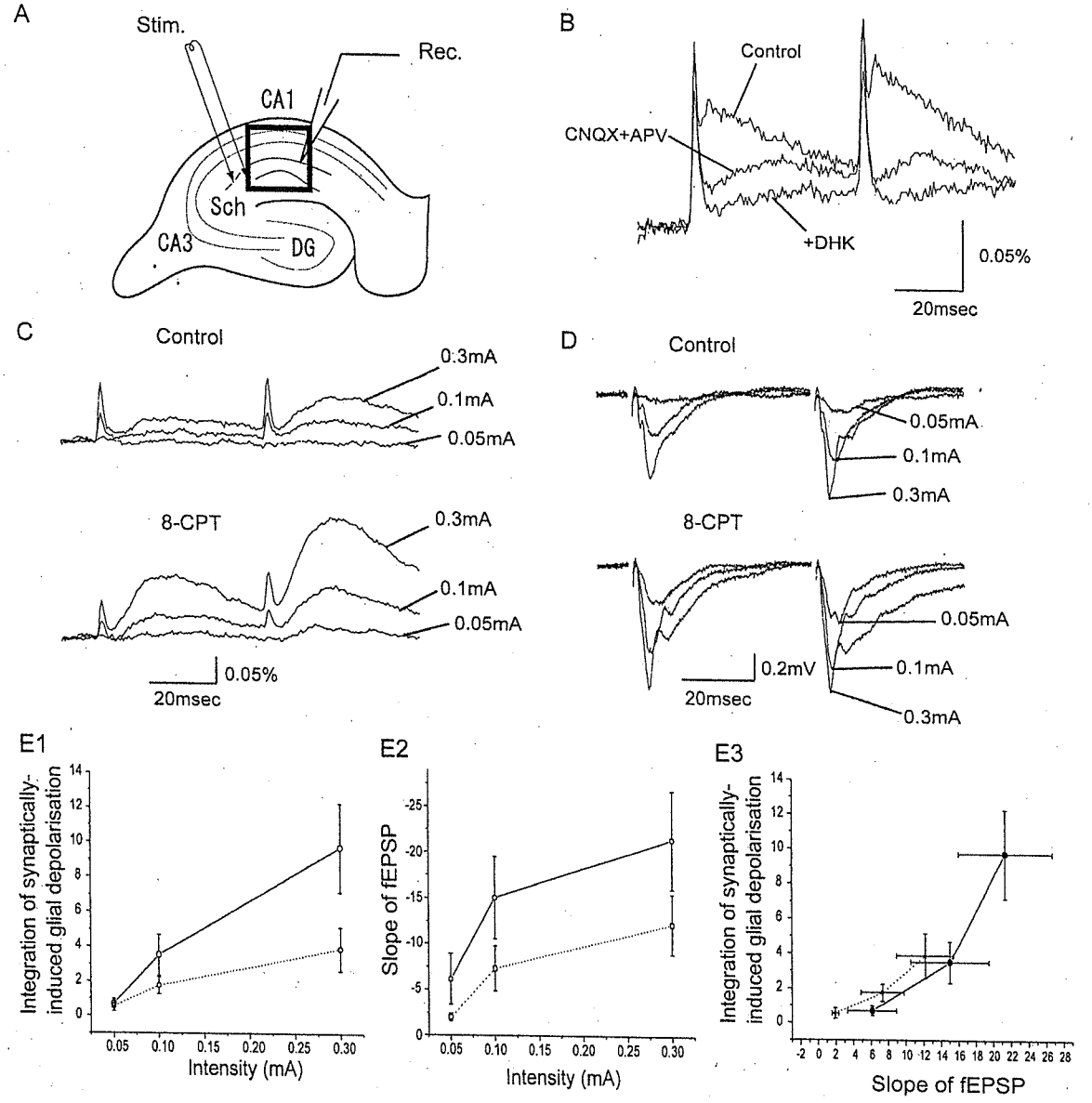

Fig. 1. Synaptically induced glial depolarisation monitored optically in the hippocampal CA1 area. (A) A slice was stained with a voltage-sensitive dye RH155. The slice was electrically stimulated by a bipolar electrode (Stim.) positioned in the stratum radiatum. An extracellular recording electrode (Rec.) was placed in the stratum radiatum to record the fEPSP. The changes in absorption were measured from the area indicated by a rectangle. (B) Sample traces of the change in absorption in response to a pair of stimuli recorded from the stratum radiatum. In control artificial cerebrospinal fluid, the response consists of three main components: a very fast spike-like component due to activity of presynaptic fiber volley, a fast component, and a slow component. Blockage of ionotropic glutamate receptors by applying CNQX (10 μM) and APV (50 μM) abolished the fast responses, leaving slow depolarising responses. Bath application of DHK (1 mM), a selective GLT-1 glutamate transporter antagonist, suppressed the synaptically induced glial depolarisation. (C, D) Synaptically induced glial depolarisation and fEPSP evoked by stimulus at various intensities (0.05–0.3 mA) in control conditions (top) and in the presence of 8-CPT (0.5 μM), a specific adenosine A_1 receptor blocker (bottom). (E1, E2) Dependence of the initial slope of the fEPSP (n=6) and the amplitude of the synaptically induced glial depolarisation (n=6) on stimulus intensity in control conditions (dashed line) and in the presence of 0.5 μM 8-CPT. (E3) The relationship between the fEPSP (n=6) and the synaptically induced glial depolarisation (n=6) at different stimulus intensities in control conditions (dashed line) and in the presence of 0.5 μM 8-CPT.

the bathing medium, then synaptically induced glial depolarisation was elicited by applying five repetitive stimuli at 10 ms intervals in order to increase the signal to noise ratio, a stimulation pattern which itself does not cause a change in the amplitude of the synaptically induced glial depolarisation (Kawamura et al., 2004). ω-AgaIVA was used to block P/Q-type channels and ω-CgTxGVIA to block N-type channels; on the basis of the results of Wu and Saggau (1994b), to obtain a maximal effect, both blockers were applied at a concentration of 1 μM for 20 min before testing for suppression of synaptically induced glial depolarisation in the presence of the voltage-gated Ca^{2+} channel blockers.

Fig. 4 shows representative responses (Fig. 4A) and the summarised results (Fig. 4B) of the effects of Ca^{2+} channel

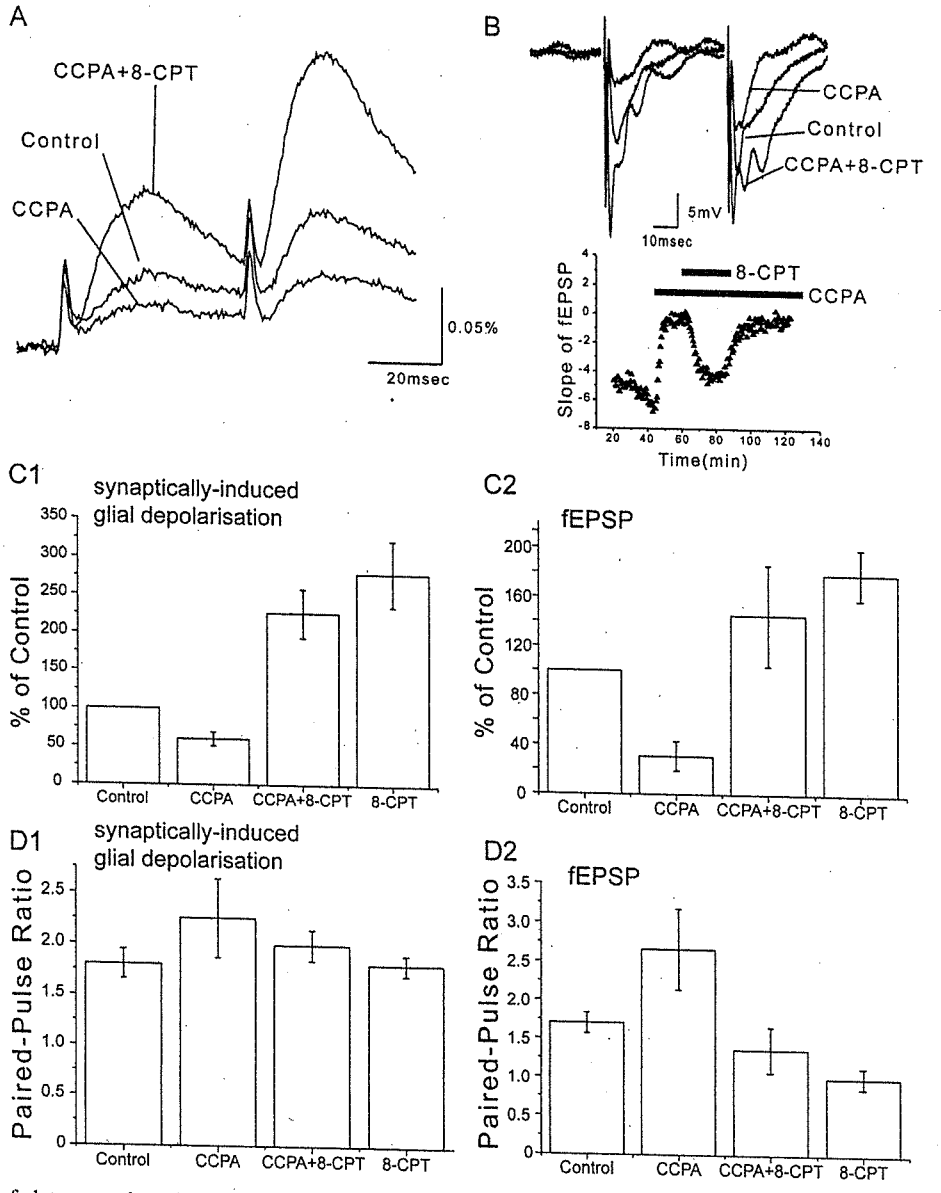

Fig. 2. Tonic inhibition of glutamate release by adenosine A_1 receptors. (A) Typical experiment showing the effects of application of CCPA (0.5 μM) and co-application of CCPA and 8-CPT (both 0.5 μM) on the synaptically induced glial depolarisation. CNQX(10 μM) and APV(50 μM) were present in the bath in all experiments. (B) Effects of application of CCPA (0.5 μM) and co-application of CCPA and 8-CPT (both 0.5 μM) on the fEPSP. Top: A typical experiment showing the field EPSPs. Bottom: Time-course of changes in the initial slope of the fEPSP during application of CCPA and co-application of CCPA and 8-CPT. Pooled data for the effects of CCPA alone and CCPA plus 8-CPT on the synaptically induced glial depolarisation (C1, n=4) and the fEPSP (C2, n=4). The signals were normalised to those before application of CCPA or 8-CPT. Effects of CCPA and co-application of CCPA and 8-CPT on the paired-pulse ratio of the synaptically induced glial depolarisation (D1) and the fEPSP (D2). Each column and bar indicates the mean and S.E.M.

blockers in the absence of 8-CPT. Both Ca^{2+} channel blockers suppressed the amplitude of the synaptically induced glial depolarisation without affecting the time-course of the effect. To estimate the relative contribution of different types of Ca^{2+} channels to transmitter release, the degree of suppression caused by a blocker of a specific Ca^{2+} channel type should be normalised to that caused by a potent non-specific Ca^{2+} channel blocker. In the presence of DHK, synaptically induced glial depolarisation was suppressed to such an extent that the addition of 300 μM Cd^{2+} to the bathing medium did not suppress the signal further (data not shown). To normalise the amplitude of the synaptically induced glial depolarisation, we therefore subtracted the amplitude of the signal obtained in the presence of DHK from that obtained in its absence.

When the adenosine A_1 receptor was not blocked, application of ω-AgaIVA (1 μM) alone, ω-CgTxGVIA (1 μM) alone or co-application of ω-AgaIVA and ω-CgTxGVIA reduced the synaptically induced glial depolarisation to 44.4±6.5% (n=10), 67.4±7.3% (n=10) or 30.3±3.6% (n=10) of control levels, respectively (Fig. 4B). In contrast, in the presence of 8-CPT (10 μM), the corresponding values were 47.9±5.9% (n=6), 32.0±5.7% (n=4) or 22.7±7.7% (n=5) of control levels (Fig. 5B).

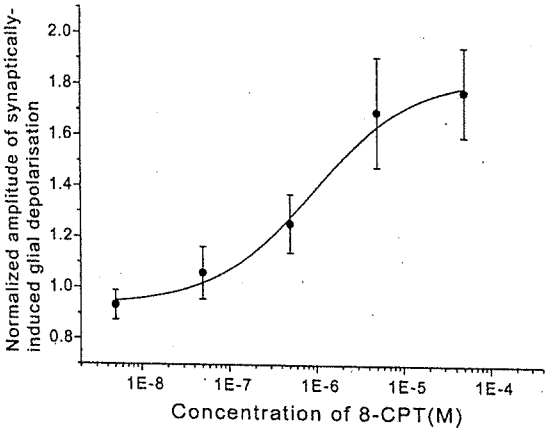

Fig. 3. Dose dependency of the effects of 8-CPT on the amplitude of the synaptically induced glial depolarisation. The amplitude of the synaptically induced glial depolarisation in the presence of 8-CPT was normalised to the value before applying 8-CPT. The bars show the S.E.M. (n=6). Data points were fitted to a sigmoidal curve (Y=[−0.9/{1+(x/EC^{50})$^{0.8}$}+1.8]) using the χ^2 method. The EC_{50} value was 0.9±1.1 μM.

These results showed that, in the presence of adenosine A_1 receptor-mediated suppression, the contribution of the P/Q-type channel was greater than that of the N-type channel, but, when adenosine A_1 receptor-mediated suppression was removed, the contribution of the N-type Ca^{2+} channel was greater than that of the P/Q-type channel.

4. Discussion

In this study, we monitored glutamate transmitter release by optically recording glial glutamate transporter activity, and found that the contribution of N-type voltage-gated Ca^{2+} channels to glutamate release was greater than that of P/Q-type voltage-gated Ca^{2+} channels when adenosine A_1 receptors were inhibited. This indicates that glutamate release at hippocampal CA3–CA1 synapse is tonically suppressed by activation of adenosine A_1 receptors and that the suppression is mainly due to inhibition of N-type voltage-gated Ca^{2+} channel.

The method we used in this study to measure glutamate release involved the monitoring of glutamate transporter activity in glial cells. We have shown in a previous report (Kojima et al., 1999) that the signal is due to glial transport on the basis that the signal can be recorded in a preparation in which postsynaptic cells are absent and that the signal was almost absent in slice preparations made from GLT-1 knock out mice. Still we cannot rule out the possibility that a

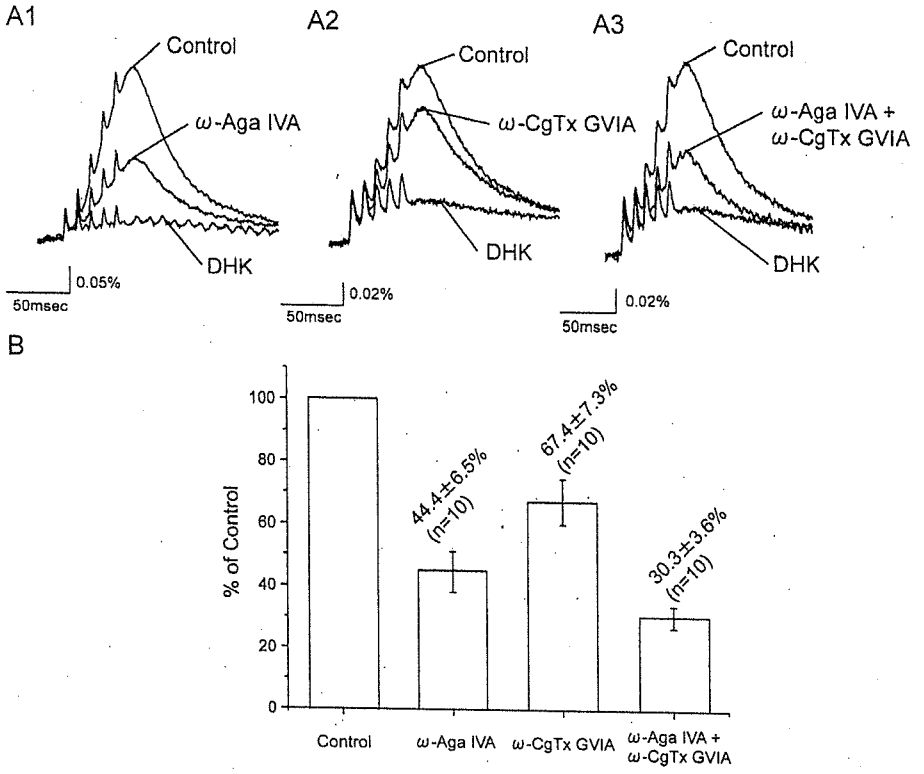

Fig. 4. Effects of Ca^{2+} channel blockers on the amplitude of the synaptically induced glial depolarisation in the absence of an adenosine A_1 receptor blocker. (A) The synaptically induced glial depolarisation was measured in normal artificial cerebrospinal fluid, and the blockers for the P/Q-type channel, ω-AgaIVA (1 μM, A1), and/or the N-type channel, ω-CgTxGVIA (1 μM, A2) were applied. Responses were evoked by delivering 5 stimuli with a 10-ms interval to Schaffer collaterals. The effect of application of ω-CgTxGVIA was smaller than that of ω-AgaIVA. Application of DHK (1 mM) suppresses the component due to glutamate uptake, leaving a component which is not related to glutamate release. CNQX (10 μM) and APV (50 μM) were present in the bath in all experiments. (B) Statistical comparison of the effects of Ca^{2+} channel blockers on the synaptically induced glial depolarisation in the absence of 8-CPT (10 μM). After subtracting the DHK-insensitive component, the signal was integrated over the first 200 ms and normalised to the value in control conditions. Each column and bar indicates the mean and S.E.M.